

# Simulation of non-Newtonian viscoplastic flows with a unified first order hyperbolic model and a structure-preserving semi-implicit scheme

Ilya Peshkov<sup>a,\*</sup>, Michael Dumbser<sup>a</sup>, Walter Boscheri<sup>b</sup>, Evgeniy Romenski<sup>c</sup>, Simone Chiochetti<sup>a</sup>, Matteo Ioriatti<sup>a</sup>

<sup>a</sup>Laboratory of Applied Mathematics, University of Trento, Via Mesiano 77, 38123 Trento, Italy

<sup>b</sup>Department of Mathematics and Computer Science, University of Ferrara, via Machiavelli 30, I-44121 Ferrara, Italy

<sup>c</sup>Sobolev Institute of Mathematics, 4 Acad. Koptug Avenue, Novosibirsk, Russia

---

## Abstract

We discuss the applicability of a unified hyperbolic model for continuum fluid and solid mechanics to modeling non-Newtonian flows and in particular to modeling the stress-driven solid-fluid transformations in flows of viscoplastic fluids, also called yield-stress fluids. In contrast to the conventional approaches relying on the non-linear viscosity concept of the Navier-Stokes theory and representation of the solid state as an infinitely rigid non-deformable solid, the solid state in our theory is deformable and the fluid state is considered rather as a “melted” solid via a certain procedure of relaxation of tangential stresses similar to Maxwell’s visco-elasticity theory. The model is formulated as a system of first-order hyperbolic partial differential equations with possibly stiff non-linear relaxation source terms. The computational strategy is based on a staggered semi-implicit scheme which can be applied in particular to low-Mach number flows as usually required for flows of non-Newtonian fluids. The applicability of the model and numerical scheme is demonstrated on a few standard benchmark test cases such as Couette, Hagen-Poiseuille, and lid-driven cavity flows. The numerical solution is compared with analytical or numerical solutions of the Navier-Stokes theory with the Herschel-Bulkley constitutive model for nonlinear viscosity.

*Keywords:* Hyperbolic equations, viscoplastic fluids, yield stress, stress relaxation, semi-implicit scheme, staggered mesh

---

## 1. Introduction

In [71, 31, 30], a unified first-order hyperbolic formulation for continuum fluid and solid mechanics was proposed. In a single system of partial differential equations (PDEs), such a model can describe various material responses including inviscid<sup>1</sup> and viscous fluids, elastic and elastoplastic solids, see also [3, 44, 68, 18]. Due to its geometric, [72] and thus intrinsically covariant nature, this model was also formulated in the general relativistic setting [74]. Another useful extension of the model is based on the coupling with the equations for continuous modeling of damage and fracture which allows to describe both ductile and brittle fractures, e.g. see [83, 40]. The model originated from the works by Godunov and Romenski on Eulerian non-linear elastoplasticity theory [45, 47, 75, 46] in 1970s. Later it was suggested by Peshkov and Romenski [71] that this theory can be applied to describe viscous Newtonian flows. Therefore, sometimes we shall refer to this model as the Godunov-Peshkov-Romenski model or GPR model.

In this paper, we focus on investigating the capabilities of the unified model to describe flows exhibiting solid-fluid-type transformations such as in flows of viscoplastic fluids [2], also called yield-stress fluids. Indeed, being able

---

\*Corresponding author

*Email address:* [ilya.peshkov@unitn.it](mailto:ilya.peshkov@unitn.it) (Ilya Peshkov)

<sup>1</sup>Of course, in the inviscid case, one can use directly the Euler equations for ideal fluids. But formally speaking, the Euler equations can be recovered in the stiff relaxation limit of the unified theory, e.g. see the asymptotic analysis in [31].

to model both fluid and solid states, this unified formulation is a good candidate for a monolithic continuous modeling of the solid-fluid transition such as thermally-driven melting and solidification<sup>2</sup> process in additive manufacturing [36, 57, 56] as well as stress-driven fluidization and solidification process in industrial and environmental flows (landslides, avalanches, lava flows) of viscoplastic fluids and of dense granular flows [1]. This paper presents a preliminary step towards this ultimate goal. In particular, we shall assume that the solid-fluid transition occurs in a time-independent manner, i.e. infinitely fast.

Under these assumptions, we found out that the unified model is able to describe a quite general theoretical class of fluid flows, called Herschel-Bulkley fluids, which unites the nonlinear power-law-type viscosity with the yield-stress behavior of Bingham-type materials. The ability of the unified model to describe flows of non-Newtonian fluids with a power-law viscosity was already demonstrated by Jackson and Nikiforakis [53]. Also, the model was used by Hank et al [49, 50] in the elastoviscoplastic regime to model high-strain-rate impact problems of clay-type materials. In this paper, the ability of the unified model to describe the yield-stress behavior of viscoplastic fluids in low-Mach number regime is discussed for the first time.

The most dramatic feature of viscoplastic fluids [2], is the *yield stress*, from both the physical and mathematical perspective, because below this threshold such a material behaves as an elastic solid (i.e. it is able to recover its original shape after the loading has been removed) while it flows irreversibly like a viscous fluid if the stresses exceed a threshold. Thus, such materials exhibit drastically different behavior above and below the yield stress.

While it is apparent that real viscoplastic fluids are essentially two-phase media with a stress-induced solid-fluid phase transformation, such materials have been considered as a two-phase media only relatively recently by Putz and Burghelca in [73] and Grmela [48]. In particular, it was demonstrated in [73] that some experimental data for a typical viscoplastic fluid such as shear thinning physical gel (Carbopol 940) can be fitted quite well if the chemical kinetics of the solid-fluid transition (i.e. breaking and restoration of bonds between molecules) are taken into account via an additional equation for the mass fraction of the solid state. Nevertheless, from the mathematical modeling viewpoint, to apply a two-phase approach to modeling viscoplastic flows is very challenging because fluids and solids are traditionally modeled by very different mathematical equations. Namely, fluid mechanics relies on the second-order Navier-Stokes equations of *parabolic* type, while solid mechanics relies on the first-order elastodynamic equations which are of *hyperbolic* type. Hence, a description of the solid-fluid transition would require changing the type of the PDEs which is a non-trivial problem from the mathematical and computational standpoints. Therefore, viscoplastic fluids are traditionally described by means of phenomenological Bingham-type models in which a material is considered as a *nondeformable* solid below the yield stress (infinitely rigid solid represented by the Navier-Stokes equations with an infinitely large viscosity), while the flow starts abruptly once the applied stress exceeds a threshold. Nevertheless, in the last couple of decades, mixed elastoviscoplastic approaches which combine the Navier-Stokes and elasticity theory have been proposed by several authors [76, 77, 4, 39]. The main idea of this type of models is to represent the Cauchy stress tensor  $\boldsymbol{\sigma}$  as the sum of two parts  $\boldsymbol{\sigma} = \boldsymbol{\sigma}_{NS}(\dot{\boldsymbol{\epsilon}}) + \boldsymbol{\sigma}_E(\boldsymbol{\epsilon})$  with  $\boldsymbol{\sigma}_{NS}(\dot{\boldsymbol{\epsilon}})$  being the conventional Navier-Stokes stress defined as the function of the strain rate  $\dot{\boldsymbol{\epsilon}}$ , and  $\boldsymbol{\sigma}_E$  being the elastic stress which is a function of the strain  $\boldsymbol{\epsilon}$ . Yet, in these approaches, the fluid and solid states are characterized by the state variables of opposite nature, i.e.  $\dot{\boldsymbol{\epsilon}}$  being non-local (needs spatial gradients of velocity) and dissipative and  $\boldsymbol{\epsilon}$  being local and non-dissipative. It is thus, not clear at all how one can build a thermodynamically consistent theory describing transformation of one into another.

In contrast to the traditional way of modeling viscoplastic flows and the new aforementioned approaches, our approach does not rely on the Navier-Stokes theory and does not consider viscous fluids as a strain-rate-type constitutive theory, i.e. the strain rate  $\dot{\boldsymbol{\epsilon}}$  is excluded from being the state variable. Instead, both solids and fluids are considered from a deformation, and thus unified, geometrical standpoint<sup>3</sup>. This, in particular, allows to use exactly the same state variables for fluids and solids and to compute the Cauchy stress tensor in a unified manner. Furthermore, instead of the traditional viscosity, the parameter that characterizes the ability of the material to flow

---

<sup>2</sup>For example, the importance of developing such an approach as ours is dictated by the necessity to predict the distribution of residual stresses in solidified materials in additive manufacturing. Recall that residual stresses can not appear in solids if they are treated as an infinitely viscous fluids.

<sup>3</sup>In the language of differential geometry, this theory can be considered as a Riemann-Cartan geometry with non-zero torsion [72].

in our theory is the strain relaxation time  $\tau$  which is a continuous analog of Frenkel’s concept of relaxation time  $\tau_F$  in liquids [38, 17, 8, 10] which was proposed by Frenkel [38] and essentially provides a solid-like view on the kinetic description of liquids, e.g. see the discussion in [30] on Frenkel’s relaxation time and its continuous interpretation in our theory. We believe that the characterization of fluids and solids by the same set of state variables, the same form of the stress tensor, and the same “fluidity” characteristic (relaxation time) have a great potential for modeling of solidification/melting processes as it provides a unified thermodynamically consistent framework for continuous tracking of material properties across<sup>4</sup> the solid-fluid transformation fronts.

Concerning our numerical strategy, in contrast to our previous papers [31, 32, 18, 68] in which the model was studied using explicit Finite Volume and Discontinuous Galerkin methods belonging to the family of high-order ADER-Finite-Volumes and ADER-Discontinuous-Galerkin schemes [88, 85, 90, 86, 89, 22, 34, 29, 33, 35] and ADER schemes in the Arbitrary Lagrangian Eulerian framework [14, 15, 16, 41, 42], in this paper, we rely on our recent Semi-Implicit Structure Preserving Finite Volume (SISPFV) scheme [13] which allows to run the model efficiently in the low-Mach number regime typical for problems involving non-Newtonian fluids.

## 2. Mathematical model

### 2.1. System of governing PDEs

A quite general mixture model for modeling stress-induced solid-fluid phase transition was proposed in [69]. In this paper, however, we consider a much simpler model. In particular, we assume that the mobility of the solid and fluid phases in the transition zone is negligible, i.e. the relative velocity of the phases is zero. Furthermore, we shall assume that the fluid and solid states are only differ by the so-called strain relaxation time  $\tau$  (to be introduced later) while all other material parameters such as longitudinal and shear sound speed<sup>5</sup> are equal.

The state parameters of interest are

$$(\rho, s, \mathbf{v}, \mathbf{A}), \tag{1}$$

where  $\rho$  is the mass density,  $s$  is the specific entropy,  $\mathbf{v}$  is the material velocity, and  $\mathbf{A}$  is the distortion matrix which characterizes the morphology of the material elements. The distortion can be seen as a local basis triad (three vectors). For example, these vectors are denoted as  $e^\beta$ ,  $\beta = 1, 2, 3$  in papers [43] by Gavriluk and Favrie. By measuring the changes in angles between these three vectors and coefficients of elongation/contraction, one can use  $\mathbf{A}$  as a deformation measure of the material elements<sup>6</sup>. Also, the word “local” means that it is impossible to recover the global deformation of the whole continuum by integrating the distortion field  $\mathbf{A}$ . The distortion matrix  $\mathbf{A}$  can be related to the elastic part  $\mathbf{F}^e$  of the deformation gradient  $\mathbf{F} = \mathbf{F}^e \mathbf{F}^p$  in the conventional finite-strain inelasticity as  $\mathbf{A} = (\mathbf{F}^e)^{-1}$ , where  $\mathbf{F}^p$  is the plastic component of the full deformation gradient  $\mathbf{F}$ . Remark that if one is working in the Eulerian frame, the plastic component  $\mathbf{F}^p$  is not required as discussed for example in [68, 69].

---

<sup>4</sup>See also further developments of Frenkel’s seminal idea in unified descriptions [52, 23, 9, 37] of thermodynamical properties of matter across the solid-fluid interfaces.

<sup>5</sup>Recall that in our theory, a viscous fluid is also characterized by a shear sound speed.

<sup>6</sup>In the language of differential geometry, the distortion field can be viewed as a non-holonomic frame field (local basis triad), or Cartan’s moving frame, e.g. see [51, 72].

The system of governing PDEs in a Cartesian coordinate system can be written as [71, 31]

$$\frac{\partial \rho}{\partial t} + \frac{\partial(\rho v_k)}{\partial x_k} = 0, \quad (2a)$$

$$\frac{\partial(\rho v_i)}{\partial t} + \frac{\partial(\rho v_i v_k + p \delta_{ki} - \sigma_{ki})}{\partial x_k} = 0, \quad (2b)$$

$$\frac{\partial A_{ik}}{\partial t} + \frac{\partial(A_{im} v_m)}{\partial x_k} + v_j \left( \frac{\partial A_{ik}}{\partial x_j} - \frac{\partial A_{ij}}{\partial x_k} \right) = -\frac{E_{A_{ik}}}{\theta}, \quad (2c)$$

$$\frac{\partial(\rho s)}{\partial t} + \frac{\partial(\rho s v_k)}{\partial x_k} = \frac{\rho}{\theta T} E_{A_{ik}} E_{A_{ik}}, \quad (2d)$$

$$\frac{\partial(\rho E)}{\partial t} + \frac{\partial(\rho E v_k + v_i(p \delta_{ki} - \sigma_{ki}))}{\partial x_k} = 0. \quad (2e)$$

where the pressure  $p$  and the tangential stresses  $\sigma_{ik}$  should be defined via the total energy potential  $E(\rho, s, \mathbf{v}, \mathbf{A})$  as  $p = \rho^2 E_\rho$  and  $\sigma_{ki} = -\rho A_{ji} E_{A_{jk}}$ , where, in turn,  $E_\rho = \frac{\partial E}{\partial \rho}$  and  $E_{A_{jk}} = \frac{\partial E}{\partial A_{jk}}$ ,  $\delta_{ki}$  is the Kronecker delta,  $T = E_s$  is the temperature, and  $\theta > 0$  is one of the main constitutive functions of our theory which controls the rate of strain relaxation and will be specified in Sec. 2.3.

System (2) is an overdetermined system which has one more equations than unknowns. In fact, the total energy  $E$  as mentioned above, is not an unknown but a potential  $E = E(\rho, s, \mathbf{v}, \mathbf{A})$  and the last equation (the total energy conservation law) is, in fact, the consequence of the others, i.e. it can be obtained as a linear combination of the other equations, e.g. see [70, 46]. Yet, in order to guarantee the energy conservation exactly at the discrete level, it is equation (2e) that is used in the discretization of system (2) while the entropy equation is obtained as a consequence, see [13].

One can see that in order to close system (2) (to specify the pressure, stress, etc) one needs to specify the energy potential  $E$  which is done in the following section.

## 2.2. Closure of the reversible part via energy potential

To close the system of governing PDEs (2), one needs to propose a model for the total energy  $E$  and the strain relaxation function  $\theta$ . Here, we specify the total energy potential as the sum of three contributions<sup>7</sup>

$$E(\rho, s, \mathbf{v}, \mathbf{A}) = E_i(\rho, s) + E_e(\mathbf{A}) + E_k(\mathbf{v}) \equiv E_i(\rho, s) + \frac{c_{\text{sh}}^2}{2} \|\mathbf{G}'\|^2 + \frac{1}{2} \|\mathbf{v}\|^2, \quad (3)$$

where  $E_i(\rho, s)$  is the internal energy of volumetric deformation,  $E_e(\mathbf{A})$  is the elastic energy of shear deformation, and  $E_k(\mathbf{v})$  is the kinetic energy,  $\mathbf{G}' = \mathbf{G} - \frac{1}{3} \text{tr}(\mathbf{G}) \mathbf{I}$  is the deviatoric (or trace-less) part of the metric tensor  $\mathbf{G} = \mathbf{A}^\top \mathbf{A}$ ,  $\mathbf{I}$  is the identity matrix, and we use the following matrix and vector norms

$$\|\mathbf{G}'\| = \sqrt{\frac{1}{2} G'_{ij} G'_{ij}}, \quad \|\mathbf{v}\| = \sqrt{v_i v_i}. \quad (4)$$

Also,  $c_{\text{sh}}$  is the shear sound speed, which, as was mentioned earlier, is assumed to be the same in the solid and fluid states. It characterizes the rigidity of the infinitesimal frames represented by the basis triads  $\mathbf{A}$ .

The internal energy  $E_i(\rho, s)$ , in the case of solids and liquids, can be taken as a stiffened gas equations of state, e.g. see [31, 13]. However, in this paper, we only consider test cases that are considered in the literature for incompressible isothermal flows in confined geometries. This means that the choice of the internal energy  $E_i(\rho, s)$

<sup>7</sup>In a general situation, the fluid and solid state of the material are governed by their own equations of state (energies)  $E_f$  and  $E_s$  so that the total energy of the material is  $E = cE_s + (1-c)E_f$  with  $c$  being the solid mass fraction governed by its own time evolution equation.

plays no role in this study. Nevertheless, in order to stay in the hyperbolic region of model (2), we always solve the full *compressible* model (2) for the full vector of state variables (1) and hence, an equations of state for the internal energy  $E_i(\rho, s)$  has to be always provided. In particular, in all the test cases, we shall use the ideal gas equation of state for  $E_i(\rho, s)$ , i.e.  $E_i(\rho, s) = \frac{\rho^{\gamma-1}}{\gamma-1} e^{s/c_v}$  or  $E_i(\rho, p) = \frac{p}{\rho(\gamma-1)}$  with  $c_v$  being the heat capacity at constant volume and  $\gamma$  the ratio of specific heats.

Remark that, when dealing with incompressible flows, we do not impose the incompressibility constraint  $\nabla \cdot \mathbf{v} = 0$ , which would change the type of the governing PDEs from hyperbolic to a mixed hyperbolic-elliptic type. Instead, we solve the full compressible formulation (2) with the new semi-implicit SISPFV scheme [13] in the low-Mach number limit  $\text{Ma} \rightarrow 0$ . Thus, as shown in [13], with this type of schemes, the density and velocity divergence fluctuations scale with  $\text{Ma}^2$  in the low-Mach number limit.

Using (3), one can explicitly compute the derivatives  $E_{A_{ik}}$  used in the right hand side of (2) and in the computation of the stress  $\sigma_{ki}$ . Thus, we have

$$E_A = c_{\text{sh}}^2 \mathbf{A} \mathbf{G}', \quad \boldsymbol{\sigma} = -\rho \mathbf{A}^\top E_A = -2\rho \mathbf{G} E_G = -\rho c_{\text{sh}}^2 \mathbf{G} \mathbf{G}'. \quad (5)$$

We remark that in contrast to the Navier-Stokes theory where the tangential stresses are of a dissipative nature, the tangential stresses of our theory are due to elastic forces which are intrinsically non-dissipative. The dissipation is introduced only via the right-hand side of system (2). In other words, in the context of viscous fluids, viscous solution of the parabolic Navier-Stokes equations is approximated by a solution of hyperbolic system (2) of visco-elastic medium, see the following section for the details.

### 2.3. Closure of the irreversible part

Recall that if the source term in (2c) vanishes then system (2) is simply the system of nonlinear elasticity written in the Eulerian coordinates [46, 31]. We thus say that the left hand-side of (2) is the reversible part of the time evolution [70, 66]. However, the most drastic change in the material behavior is controlled by the right hand-side of (2c) which, together with the entropy production source term in (2d), constitutes the irreversible (dissipative) part of the time evolution. Note that the entropy production source term is obviously positive and hence, the second law of thermodynamics is always respected [70].

In particular, denoting by  $\tau$  the strain relaxation time discussed in the introduction and taking the energy potential in the form (3) and  $\theta$  in the form

$$\theta = \frac{1}{3} \tau c_{\text{sh}}^2 |\mathbf{A}|^{-5/3}, \quad (6)$$

it has been shown in [71, 31] that, for small  $0 < \tau \ll 1$ , the stress tensor of our theory  $\boldsymbol{\sigma} = -\rho \mathbf{A}^\top E_A$  (which is computed fully locally, i.e. as an algebraic function of state variables) approximates the Navier-Stokes stress (which is non-local in space, i.e. its computation involves spatial derivatives)

$$\boldsymbol{\sigma}_{NS} = \eta \dot{\boldsymbol{\gamma}}, \quad \dot{\boldsymbol{\gamma}} = \dot{\boldsymbol{\varepsilon}} - \frac{1}{3} \text{tr}(\dot{\boldsymbol{\varepsilon}}) \mathbf{I}, \quad \dot{\boldsymbol{\varepsilon}} = \nabla \mathbf{v} + \nabla \mathbf{v}^\top, \quad (7)$$

at first order in  $\tau$ , i.e. one can expand  $\boldsymbol{\sigma}$  in series in  $\tau$

$$\boldsymbol{\sigma} = \boldsymbol{\sigma}_0 + \tau \boldsymbol{\sigma}_1 + \tau^2 \boldsymbol{\sigma}_2 + \dots \quad (8)$$

such that  $\boldsymbol{\sigma}_0 = \mathbf{0}$  and

$$\boldsymbol{\sigma}_1 = \frac{1}{6} \rho \tau c_{\text{sh}}^2 \dot{\boldsymbol{\gamma}}. \quad (9)$$

Here,  $\frac{1}{2} \dot{\boldsymbol{\varepsilon}}$  is the strain rate tensor and  $\dot{\boldsymbol{\gamma}}$  is the rate-of-shear tensor.

Thus, by comparing (7) and (9), one can conclude that the *effective* shear viscosity of our theory is expressed as<sup>8</sup>

$$\eta_{\text{eff}} = \frac{1}{6} \rho \tau c_{\text{sh}}^2. \quad (10)$$

---

<sup>8</sup>This formula for  $\eta_{\text{eff}}$  is valid only for the energy given by (3) and  $\theta$  given by (6). For a different energy potential and  $\theta$ , the coefficient  $\frac{1}{6}$  may change or may depend on the density  $\rho$  and entropy  $s$ . Nevertheless, in general, one has that  $\eta_{\text{eff}} \sim \rho \tau c_{\text{sh}}^2$ .

One can clearly see that the effective viscosity  $\eta_{eff}$  is composed of the two principal parameters of our theory: the shear sound speed  $c_{sh}$  which characterizes the elasticity of the infinitesimal frames represented by the basis triads  $\mathbf{A}$  and thus, characterizes the reversible part of the model, and  $\tau$  which characterizes the rate of dissipation. In other words, even if the model is employed in the diffusive regime<sup>9</sup> ( $\tau \ll 1$ ), the viscous flow is approximated by a *viscoelastic* solution of our theory. In this case, the dissipative dynamics governed by the right hand-side dominates.

Therefore, in the presence of the relaxation term in (2c), the overall dynamics of system (2) is always of viscoelastic type at the time scales  $\tau < t < \infty$  because both parts of the time evolution (left and right hand-sides of (2)) are working together. Yet, the dynamics is reversible (elastic) at the time scales  $t < \tau$ , e.g. see [38, 17, 8, 10, 71].

Despite the asymptotic expansion (8) being only performed under the assumptions of constant viscosity and constant relaxation time, we shall assume<sup>10</sup> in this paper that the same procedure can be done even in the case of nonlinear viscosity which will inevitably result in a nonlinear but still sufficiently small  $\tau$ , now being a function of state variables  $\tau = \tau(\rho, s, \mathbf{A})$ . In principle, the “*sufficient smallness*” of  $\tau$  can be achieved by taking larger shear sound speed  $c_{sh}$  that for the same viscosity provides a smaller  $\tau$  as can be seen from (10).

### 2.3.1. Pure fluids (no yield-stress behavior)

Based on the aforementioned reasoning, we assume that if the Newton law of viscosity (7) is generalized with a nonlinear viscosity

$$\boldsymbol{\sigma}_{NS} = \eta(\dot{\gamma}) \dot{\boldsymbol{\gamma}}, \quad \dot{\gamma} = \|\dot{\boldsymbol{\gamma}}\| = \sqrt{\frac{1}{2} \dot{\gamma}_{ij} \dot{\gamma}_{ij}}, \quad (11)$$

we still assume that the relation (10) holds for some constant shear sound speed  $c_{sh}$  and some nonlinear function  $\tau(\mathbf{A})$  to be determined.

For example, for incompressible flows of the power-law (PL) fluids with the viscosity

$$\eta_{PL}(\dot{\gamma}) = \kappa \dot{\gamma}^{n-1}, \quad (12)$$

with  $\kappa$  and  $n$  being the so-called consistency and power-law indexes, one should solve (11) with respect to  $\dot{\gamma}$ , i.e.  $\dot{\gamma}(\sigma) = (\sigma/\kappa)^{1/n}$ , where  $\sigma = \|\boldsymbol{\sigma}\|$ . This is necessary because  $\dot{\boldsymbol{\gamma}}$  is not a state variable in our theory. Then, one can get the power-law viscosity as a function of  $\sigma$  which, in turn, is the function of  $\mathbf{A}$ :

$$\eta_{PL}(\mathbf{A}) = \kappa \left( \frac{\sigma}{\kappa} \right)^{\frac{n-1}{n}} \quad (13)$$

and the corresponding relaxation time  $\tau$  is simply obtained from (10) and (13) as  $\tau(\mathbf{A}) = 6 \eta_{PL}(\mathbf{A}) / (\rho c_{sh}^2)$ . Remark that the relation (13) can be recognized as a Perzyna-type model [54, 67]. In particular, in this way, the first results for non-Newtonian power-law fluids with model (2) were obtained in [53] for Hagen-Poiseuille and lid-driven cavity flows.

Note that not all rheological models can be formulated in simple linear form as (11), e.g. see [61], and here, we do not provide a general recipe for finding the proper expression for the relaxation time  $\tau$ . For a specific nonlinear stress-strain-rate relation of the form  $f(\boldsymbol{\sigma}, \dot{\boldsymbol{\gamma}}) = 0$ , this question should be considered individually.

### 2.3.2. Viscoplastic fluids

In the classical fluid mechanics models such as Bingham, or more general Herschel-Bulkley model with yield-stress behavior, the material in the solid state is traditionally treated as a *rigid solid* (non-deformable) which has an infinite viscosity. Thus, if we apply directly the above approach to a constitutive relation with an infinite viscosity, we obtain an infinite relaxation time  $\tau$  and therefore the smallness assumption under which the relation (10) was obtained does not hold.

<sup>9</sup>More rigorously, in the viscous regime, the relaxation time  $\tau$  has to be sufficiently smaller than the characteristic time of the macroscopic process.

<sup>10</sup>The validity of this assumption will be justified latter via numerical examples.

In fact, an infinite relaxation time in our model corresponds to a *deformable* elastic solid (the right-hand side in (2c) vanishes) and there is no need to treat it as a fluid with an infinite viscosity. Therefore, for a viscoplastic fluid with a yield-stress  $\sigma_Y$ , we shall assume smallness of  $\tau(\mathbf{A})$  only in the fluid region (i.e.  $\sigma > \sigma_Y$ ), while in the solid region ( $\sigma < \sigma_Y$ ) the relation (10) is not required and thus smallness of  $\tau$  is not required as well. This inevitably causes that in a certain vicinity of the yield-stress  $\sigma_Y$  there is a transition zone where  $\tau$  is not small and the material is neither viscous nor elastic but visco-elastic. However, as we shall see in Section 4, this zone is negligibly small and does not affect much the overall solution.

Therefore, we treat the viscoplastic fluids as elastoviscoplastic with the relaxation time given by

$$\tau(\mathbf{A}) = \begin{cases} \tau_s, & \|\boldsymbol{\sigma}\| < \sigma_Y, \\ \tau_f(\mathbf{A}), & \|\boldsymbol{\sigma}\| \geq \sigma_Y, \end{cases} \quad (14)$$

where  $\tau_s = \text{const}$  denotes the relaxation time in the solid region which is assumed to be elastic. This means that<sup>11</sup>  $\tau_s = \infty$  and the source term in (2c) simply vanishes  $\theta^{-1}E_{A_{ik}} = 0$ . The relaxation time in the fluid state  $\tau_f(\mathbf{A})$  can be computed from the viscosity based on the relation (10).

As an example, let us consider the Herschel-Bulkley (HB) constitutive relation for incompressible flows (e.g. see [54]) which includes the Bingham-type behavior

$$\dot{\boldsymbol{\gamma}} = \begin{cases} 0, & \|\boldsymbol{\sigma}\| < \sigma_Y, \\ \eta_{HB}^{-1} \boldsymbol{\sigma}, & \|\boldsymbol{\sigma}\| \geq \sigma_Y, \end{cases} \quad (15)$$

where  $\eta_{HB} = \eta_{HB}(\dot{\boldsymbol{\gamma}})$  is the Herschel-Bulkley viscosity of the fluid state that reads

$$\eta_{HB}(\dot{\boldsymbol{\gamma}}) = \kappa \dot{\boldsymbol{\gamma}}^{n-1} + \sigma_Y \dot{\boldsymbol{\gamma}}^{-1}, \quad \dot{\boldsymbol{\gamma}} = \|\dot{\boldsymbol{\gamma}}\|, \quad (16)$$

or

$$\eta_{HB}(\sigma) = \left( \frac{\sigma - \sigma_Y}{\kappa} \right)^{-\frac{1}{n}} \sigma, \quad \sigma = \|\boldsymbol{\sigma}\|, \quad (17)$$

where  $\kappa = \text{const}$  is the consistency index and  $n$  is the power-law index. Note that (16) includes the power-law viscosity (12) as a particular case for  $\sigma_Y = 0$ . Then, the fluid state relaxation time is computed from (10) as

$$\tau_f(\mathbf{A}) = \frac{6\eta_{HB}(\sigma)}{\rho c_{sh}^2}. \quad (18)$$

This strategy is employed in the numerical examples presented in the following section. Note that equations (2) with a constitutive relation similar to (14), (18) was used in [50] for impact dynamics modeling of a bentonite clay suspension which is also considered as a elastoviscoplastic-type material. Here, however, we focus on applying these constitutive relations to modeling *flow phenomena* in viscoplastic materials.

*Remark.* The solid-fluid transition as it is treated in the Bingham-type models of classical fluid mechanics is a time-independent (instantaneous) transition. However, some real complex fluids with a yield-stress behavior can not be treated in such a simplified way. The solid-fluid transition in such fluids is time-dependent and requires a chemical kinetics-type time evolution equation for an order parameter (e.g. mass fraction of the solid state) [73]. Therefore, we remark that a more general constitutive framework can be adopted in our theory for modeling this and other solid-fluid transitions, e.g. thermally driven phase transformations such as melting and solidification. In these settings, the material can be considered as a mixture of the solid and fluid states with an order-parameter-dependent relaxation time and the elastic modulus, e.g.  $\tau(c) = (c/\tau_s + (1-c)/\tau_f)^{-1}$ , where  $c$  is the mass fraction of the solid state, and  $\tau_s$  and  $\tau_f$  are the relaxation times in the solid and fluid states. In particular, a similar approach has been applied to modeling of the brittle and ductile fracture in solids in [83, 40] where the damaged material is treated as a fluid or solid with degraded elastic modulus and relaxation times.

---

<sup>11</sup>In practice, it is sufficient to take  $\tau_s$  just as a very large number (sufficiently larger than the typical time scale of the problem). In the simulations, we take  $\tau_s = 10^{20}$ .

### 3. Numerical scheme

Here, we describe the Semi-Implicit Structure Preserving Finite Volume (SISPFV) scheme [13] which is used in the numerical simulations in Section 4. The SISPFV scheme is first-order accurate in time and second-order accurate in space. It is based on the staggered discretization with the pressure and energy stored in the cell-centers, velocity field stored on the cell-edges and the distortion field in the cell-corners, see Fig. 1. The SISPFV scheme consists of four steps. In the first step, see Sec. 3.2, the nonlinear convective part of the fluxes is discretized in an *explicit* manner using a classical second order MUSCL-Hancock type TVD finite volume scheme [87]. In the second step, the distortion field is evolved according to the new *curl-preserving* explicit finite difference discretization. In the third step, the mildly nonlinear pressure sub-system (momentum and energy fluxes containing the pressure) is solved *implicitly* using the nested Newton method of Casulli and Zanolli [24, 25, 28]. And in the fourth step, the stiff source term in (2c) is treated using the implicit Euler method. Thanks to the implicit treatment of the pressure sub-system, the CFL condition for the time step is formulated based on the flow velocity  $\mathbf{v}$  and shear sound speed  $c_{\text{sh}}$  and not on the adiabatic sound speed. For semi-implicit schemes on unstructured staggered meshes, the reader is referred to [81, 82, 20, 5, 19, 21] and references therein.

The scheme is consistent with the low Mach number limit of the GPR equations, it is exactly curl-free for the homogeneous part of the PDE system in the absence of source terms and is consistent with the Navier-Stokes limit of the model in the stiff relaxation limit when  $\tau \rightarrow 0$  and with the large-strain hyperelasticity limit of the equations when  $\tau \rightarrow \infty$ . Yet, due to the strong non-linearity of the relaxation source term, the current version of the scheme is not truly asymptotic-preserving in the limit  $\tau \rightarrow 0$  for the stress tensor  $\boldsymbol{\sigma}$  but only *quasi* asymptotic-preserving, i.e. up to the second order error terms. In particular, this imposes certain limitations when we shall consider very stiff examples in Section 4, e.g. lid-driven cavity flows of HB fluid with  $n = 0.5$ .

System (2) can be written more compactly in the following matrix-vector notation

$$\frac{\partial \mathbf{Q}}{\partial t} + \nabla \cdot \mathbf{F}(\mathbf{Q}) + \mathbf{B}(\mathbf{Q}) \cdot \nabla \mathbf{Q} = \mathbf{S}(\mathbf{Q}), \quad (19)$$

with the state vector  $\mathbf{Q} = (\rho, \rho v_i, A_{ik}, \rho E)^\top$ , the nonlinear flux tensor  $\mathbf{F}(\mathbf{Q}) = (\mathbf{f}(\mathbf{Q}), \mathbf{g}(\mathbf{Q}))$ , with  $\mathbf{f}$  and  $\mathbf{g}$  the fluxes in  $x$  and  $y$  direction, respectively, the non-conservative product  $\mathbf{B}(\mathbf{Q}) \cdot \nabla \mathbf{Q}$  containing the curl terms in (2c), and the vector of potentially stiff algebraic relaxation source terms  $\mathbf{S}(\mathbf{Q})$ . As proposed in [28, 27] we *split* the flux tensor  $\mathbf{F}(\mathbf{Q})$  into a convective part and a pressure part. However, the equations for the distortion  $A_{ik}$  as well as its respective contributions to the momentum equation and to the total energy conservation law need a special *compatible* and structure-preserving discretization using a vertex-based grid staggering. Hence, (19) is rewritten as

$$\frac{\partial \mathbf{Q}}{\partial t} + \nabla \cdot (\mathbf{F}_c(\mathbf{Q}_c) + \mathbf{F}_p(\mathbf{Q}) + \mathbf{F}_v(\mathbf{Q})) + \nabla \mathbf{G}_v(\mathbf{Q}) + \mathbf{B}_v(\mathbf{Q}) \cdot \nabla \mathbf{Q} = \mathbf{S}(\mathbf{Q}), \quad (20)$$

where

$$\mathbf{F}_c = \begin{pmatrix} \rho v_k \\ \rho v_i v_k \\ 0 \\ \rho v_k (E_e + E_k) \end{pmatrix}, \quad \mathbf{Q}_c = \begin{pmatrix} \rho \\ \rho v_i \\ 0 \\ \rho (E_e + E_k) \end{pmatrix}, \quad \mathbf{F}_p = \begin{pmatrix} 0 \\ p \delta_{ik} \\ 0 \\ h \rho v_k \end{pmatrix}, \quad \mathbf{F}_v = \begin{pmatrix} 0 \\ -\sigma_{ik} \\ 0 \\ -v_i \sigma_{ik} \end{pmatrix}, \quad (21)$$

and

$$\mathbf{G}_v(\mathbf{Q}) = \begin{pmatrix} 0 \\ 0 \\ A_{im} v_m \\ 0 \end{pmatrix}, \quad \mathbf{B}_v(\mathbf{Q}) \cdot \nabla \mathbf{Q} = \begin{pmatrix} 0 \\ 0 \\ v_m \left( \frac{\partial A_{ik}}{\partial x_m} - \frac{\partial A_{im}}{\partial x_k} \right) \\ 0 \end{pmatrix}. \quad (22)$$

Here,  $h = E_i + p/\rho$  is the specific enthalpy,  $\mathbf{F}_c(\mathbf{Q}_c)$  refers to purely convective fluxes that will be discretized explicitly and  $\mathbf{F}_p(\mathbf{Q})$  are the pressure fluxes that will be discretized implicitly using an edge-based staggered grid. The resulting splitting into pressure and convective fluxes is identical to the flux-vector splitting scheme of Toro and Vázquez-Cendón forwarded in [91]. The remaining terms  $\mathbf{F}_v(\mathbf{Q})$ ,  $\nabla \mathbf{G}_v(\mathbf{Q})$  and  $\mathbf{B}_v(\mathbf{Q}) \cdot \nabla \mathbf{Q}$  will be carefully



discretized in a structure-preserving manner using an explicit scheme on an appropriate vertex-based staggered grid. The relaxation source terms  $\mathbf{S}(\mathbf{Q})$  can become stiff and thus require an implicit discretization on the vertex-based staggered mesh.

The following subsystem

$$\frac{\partial \mathbf{Q}}{\partial t} + \nabla \cdot (\mathbf{F}_c(\mathbf{Q}_c) + \mathbf{F}_v(\mathbf{Q})) + \nabla \mathbf{G}_v(\mathbf{Q}) + \mathbf{B}_v(\mathbf{Q}) \cdot \nabla \mathbf{Q} = \mathbf{S}(\mathbf{Q}), \quad (23)$$

will be discretized explicitly, apart from the potentially stiff algebraic source terms in  $\mathbf{S}$ , which are discretized implicitly with a simple backward Euler scheme. The discretization method presented in the next section will consist in a combination of a classical second order MUSCL-Hancock type [87] TVD finite volume scheme for the convective fluxes  $\mathbf{F}_c$ , a curl-free discretization for the terms  $\mathbf{G}_v$  and  $\mathbf{B}_v \cdot \nabla \mathbf{Q}$  using compatible gradient and curl operators as well as a vertex-based discretization of the terms  $\mathbf{F}_v$ . The eigenvalues of subsystem (23) in  $x$  direction, or more precisely the eigenvalues of the matrix  $\mathbf{A}_v(\mathbf{Q}) \cdot \mathbf{e}_x$  with  $\mathbf{e}_x = (1, 0)$  when rewriting (23) in quasi-linear form  $\partial_t \mathbf{Q} + \mathbf{A}_v(\mathbf{Q}) \cdot \nabla \mathbf{Q} = \mathbf{S}(\mathbf{Q})$ , are

$$\lambda_{1,2}^{c,v} = u \pm \frac{2}{3} \sqrt{3} c_s, \quad \lambda_{3,4,5,6}^{c,v} = u \pm c_s, \quad \lambda_{7,8,\dots,15}^{c,v} = u. \quad (24)$$

The remaining pressure subsystem, which will be discretized implicitly, reads as follows:

$$\frac{\partial \mathbf{Q}}{\partial t} + \nabla \cdot \mathbf{F}_p(\mathbf{Q}) = 0. \quad (25)$$

As already mentioned before, the resulting pressure subsystem is formally identical to the Toro-Vázquez pressure system [91], hence its eigenvalues in  $x$  direction are

$$\lambda_{1,2}^p = \frac{1}{2} \left( u \pm \sqrt{u^2 + 4c_0^2} \right), \quad \lambda_{3,4,5,\dots,15}^p = 0, \quad (26)$$

with the adiabatic sound speed  $c_0$ , e.g. for the ideal gas EOS one has, as usual,  $c_0^2 = \gamma p / \rho$ .

### 3.1. Staggered mesh

To simplify the description of the numerical scheme, we restrict the discussion to two-dimensional motion, i.e. we assume that  $\frac{\partial}{\partial x_3}$  vanishes for all fields and thus, we assume a two-dimensional physical domain  $\Omega$  spread in  $x_1 = x$  and  $x_2 = y$  and which is covered by a set of equidistant and non-overlapping Cartesian control volumes  $\Omega^{p,q} = [x^{p-\frac{1}{2}}, x^{p+\frac{1}{2}}] \times [y^{q-\frac{1}{2}}, y^{q+\frac{1}{2}}]$  with uniform mesh spacings  $\Delta x = x^{p+\frac{1}{2}} - x^{p-\frac{1}{2}}$  and  $\Delta y = y^{q+\frac{1}{2}} - y^{q-\frac{1}{2}}$  in  $x$  and  $y$  direction, respectively, and with  $x^{p\pm\frac{1}{2}} = x^p \pm \Delta x/2$  and  $y^{q\pm\frac{1}{2}} = y^q \pm \Delta y/2$ . Nevertheless, we keep all third components of vectors and tensors in the discussion. The 3D extension of the scheme is straightforward, defining the normal components of the velocity field on the faces, and keeping the discrete distortion field  $\mathbf{A}$  in the vertices of the primary control volumes. We will furthermore use the notation  $\mathbf{e}_x = (1, 0, 0)$ ,  $\mathbf{e}_y = (0, 1, 0)$  and  $\mathbf{e}_z = (0, 0, 1)$  for the unit vectors pointing into the directions of the Cartesian coordinate axes. Also, we use the following notations for the velocity components  $u = v_1$  and  $v = v_2$ .

To avoid confusion between tensor indices and discretization indices, throughout this paper we will use the *subscripts*  $i, j, k, l, m$  for *tensor indices* and the *superscripts*  $n, p, q, r, s$  for the *discretization indices* in time and space, respectively. The discrete spatial coordinates will be denoted by  $x^p$  and  $y^q$ , while the set of discrete times will be denoted by  $t^n$ . For a sketch of the employed staggered grid arrangement of the main quantities, see Fig. 1.

### 3.2. Explicit discretization of the nonlinear convective terms and of the corner fluxes

The semi-implicit scheme used in this paper and proposed in [13] applies an explicit discretization of the nonlinear convective terms contained in  $\mathbf{F}_c = (\mathbf{F}_c(\mathbf{Q}), \mathbf{g}_c(\mathbf{Q}))$  and of the corner (vertex) fluxes  $\mathbf{F}_v = (\mathbf{F}_v(\mathbf{Q}), \mathbf{g}_v(\mathbf{Q}))$ , starting

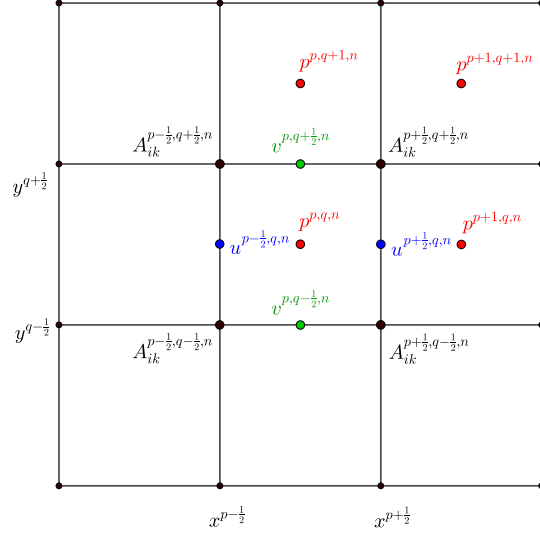


Figure 1: Staggered mesh configuration with the pressure field  $p^{p,q,n}$  defined in the cell barycenters, the velocity field components  $u^{p+\frac{1}{2},q,n}$  and  $v^{p,q+\frac{1}{2},n}$  defined on the edge-based staggered dual grids, respectively, and the distortion field  $A_{ik}^{p+\frac{1}{2},q+\frac{1}{2},n}$ .

from the known solution  $\mathbf{Q}^{p,q,n}$  at time  $t^n$ . The result is a new intermediate state vector  $\mathbf{Q}^{p,q,*}$  that is computed via a conservative finite volume formulation

$$\mathbf{Q}^{p,q,*} = \mathbf{Q}^{p,q,n} - \frac{\Delta t}{\Delta x} \left( \mathbf{F}_{c,v}^{p+\frac{1}{2},q} - \mathbf{F}_{c,v}^{p-\frac{1}{2},q} \right) - \frac{\Delta t}{\Delta y} \left( \mathbf{g}_{c,v}^{p,q+\frac{1}{2}} - \mathbf{g}_{c,v}^{p,q-\frac{1}{2}} \right), \quad (27)$$

with the numerical fluxes defined as

$$\begin{aligned} \mathbf{F}_{c,v}^{p+\frac{1}{2},q} &= u^{p+\frac{1}{2},q,n} \frac{1}{2} \left( \mathbf{Q}_c \left( \mathbf{Q}_-^{p+\frac{1}{2},q,n+\frac{1}{2}} \right) + \mathbf{Q}_c \left( \mathbf{Q}_+^{p+\frac{1}{2},q,n+\frac{1}{2}} \right) \right) - \frac{1}{2} s_{\max}^x \left( \mathbf{Q}_+^{p+\frac{1}{2},q,n+\frac{1}{2}} - \mathbf{Q}_-^{p+\frac{1}{2},q,n+\frac{1}{2}} \right) \\ &\quad + \frac{1}{2} \left( \mathbf{F}_v \left( \mathbf{Q}^{p+\frac{1}{2},q+\frac{1}{2},n} \right) + \mathbf{F}_v \left( \mathbf{Q}^{p+\frac{1}{2},q-\frac{1}{2},n} \right) \right), \end{aligned} \quad (28)$$

and

$$\begin{aligned} \mathbf{g}_{c,v}^{p,q+\frac{1}{2}} &= v^{p,q+\frac{1}{2},n} \frac{1}{2} \left( \mathbf{Q}_c \left( \mathbf{Q}_-^{p,q+\frac{1}{2},n+\frac{1}{2}} \right) + \mathbf{Q}_c \left( \mathbf{Q}_+^{p,q+\frac{1}{2},n+\frac{1}{2}} \right) \right) - \frac{1}{2} s_{\max}^y \left( \mathbf{Q}_+^{p,q+\frac{1}{2},n+\frac{1}{2}} - \mathbf{Q}_-^{p,q+\frac{1}{2},n+\frac{1}{2}} \right) \\ &\quad + \frac{1}{2} \left( \mathbf{g}_v \left( \mathbf{Q}^{p+\frac{1}{2},q+\frac{1}{2},n} \right) + \mathbf{g}_v \left( \mathbf{Q}^{p-\frac{1}{2},q+\frac{1}{2},n} \right) \right). \end{aligned} \quad (29)$$

Note that the fluxes above contain the nonlinear convective terms as well as the vertex fluxes  $\mathbf{F}_v$  and  $\mathbf{g}_v$ , which contain the stress tensor  $\boldsymbol{\sigma}$ . In (28) and (29), the maximum signal speeds are computed as

$$\begin{aligned} s_{\max}^x &= \max \left( \left\| \boldsymbol{\Lambda}_x^{c,v} \left( \mathbf{Q}_-^{p+\frac{1}{2},q,n+\frac{1}{2}} \right) \right\|, \left\| \boldsymbol{\Lambda}_x^{c,v} \left( \mathbf{Q}_+^{p+\frac{1}{2},q,n+\frac{1}{2}} \right) \right\| \right), \\ s_{\max}^y &= \max \left( \left\| \boldsymbol{\Lambda}_y^{c,v} \left( \mathbf{Q}_-^{p,q+\frac{1}{2},n+\frac{1}{2}} \right) \right\|, \left\| \boldsymbol{\Lambda}_y^{c,v} \left( \mathbf{Q}_+^{p,q+\frac{1}{2},n+\frac{1}{2}} \right) \right\| \right), \end{aligned} \quad (30)$$

with  $\boldsymbol{\Lambda}_k^{c,v}$  the diagonal matrix of eigenvalues of the explicit subsystem (23) in direction  $x$  and  $y$ , respectively. In (30)  $\|\boldsymbol{\Lambda}\|$  means the maximum norm of the matrix  $\boldsymbol{\Lambda}$ , i.e. the maximum absolute value of the matrix. The boundary-extrapolated values are simply computed via a standard MUSCL-Hancock scheme (see [87]), as follows:

$$\begin{aligned} \mathbf{Q}_-^{p+\frac{1}{2},q,n+\frac{1}{2}} &= \mathbf{Q}^{p,q,n} + \frac{1}{2} \Delta x \partial_x^h \mathbf{Q}^{p,q,n} + \frac{1}{2} \Delta t \partial_t^h \mathbf{Q}^{p,q,n}, \\ \mathbf{Q}_+^{p+\frac{1}{2},q,n+\frac{1}{2}} &= \mathbf{Q}^{p+1,q,n} - \frac{1}{2} \Delta x \partial_x^h \mathbf{Q}^{p+1,q,n} + \frac{1}{2} \Delta t \partial_t^h \mathbf{Q}^{p+1,q,n}, \end{aligned}$$

and

$$\begin{aligned}\mathbf{Q}_-^{p,q+\frac{1}{2},n+\frac{1}{2}} &= \mathbf{Q}^{p,q,n} + \frac{1}{2}\Delta y \partial_y^h \mathbf{Q}^{p,q,n} + \frac{1}{2}\partial_t \mathbf{Q}^{p,q,n}, \\ \mathbf{Q}_+^{p,q+\frac{1}{2},n+\frac{1}{2}} &= \mathbf{Q}^{p,q+1,n} - \frac{1}{2}\Delta y \partial_y^h \mathbf{Q}^{p,q+1,n} + \frac{1}{2}\partial_t \mathbf{Q}^{p,q+1,n},\end{aligned}$$

with the discrete gradients in space and time computed via

$$\begin{aligned}\partial_x^h \mathbf{Q}^{p,q,n} &= \text{minmod} \left( \frac{\mathbf{Q}^{p+1,q,n} - \mathbf{Q}^{p,q,n}}{\Delta x}, \frac{\mathbf{Q}^{p,q,n} - \mathbf{Q}^{p-1,q,n}}{\Delta x} \right), \\ \partial_y^h \mathbf{Q}^{p,q,n} &= \text{minmod} \left( \frac{\mathbf{Q}^{p+1,q,n} - \mathbf{Q}^{p,q,n}}{\Delta y}, \frac{\mathbf{Q}^{p,q,n} - \mathbf{Q}^{p-1,q,n}}{\Delta y} \right),\end{aligned}$$

and

$$\begin{aligned}\partial_t^h \mathbf{Q}^{p,q,n} &= - \frac{\mathbf{F}_c \left( \mathbf{Q}^{p,q,n} + \frac{1}{2}\Delta x \partial_x^h \mathbf{Q}^{p,q,n} \right) - \mathbf{F}_c \left( \mathbf{Q}^{p,q,n} - \frac{1}{2}\Delta x \partial_x^h \mathbf{Q}^{p,q,n} \right)}{\Delta x} \\ &\quad - \frac{\mathbf{F}_v \left( \mathbf{Q}^{p+\frac{1}{2},q+\frac{1}{2},n} \right) + \mathbf{F}_v \left( \mathbf{Q}^{p+\frac{1}{2},q-\frac{1}{2},n} \right) - \mathbf{F}_v \left( \mathbf{Q}^{p-\frac{1}{2},q+\frac{1}{2},n} \right) + \mathbf{F}_v \left( \mathbf{Q}^{p-\frac{1}{2},q-\frac{1}{2},n} \right)}{2\Delta x} \\ &\quad - \frac{\mathbf{g}_c \left( \mathbf{Q}^{p,q,n} + \frac{1}{2}\Delta y \partial_y^h \mathbf{Q}^{p,q,n} \right) - \mathbf{g}_c \left( \mathbf{Q}^{p,q,n} - \frac{1}{2}\Delta y \partial_y^h \mathbf{Q}^{p,q,n} \right)}{\Delta y} \\ &\quad - \frac{\mathbf{g}_v \left( \mathbf{Q}^{p+\frac{1}{2},q+\frac{1}{2},n} \right) + \mathbf{g}_v \left( \mathbf{Q}^{p-\frac{1}{2},q+\frac{1}{2},n} \right) - \mathbf{g}_v \left( \mathbf{Q}^{p+\frac{1}{2},q-\frac{1}{2},n} \right) - \mathbf{g}_v \left( \mathbf{Q}^{p-\frac{1}{2},q-\frac{1}{2},n} \right)}{2\Delta y}.\end{aligned}$$

### 3.3. Discrete divergence, curl and gradient operators

The main ingredients of the new structure-preserving staggered semi-implicit scheme proposed in this paper are the definitions of appropriate discrete divergence, gradient and curl operators acting on quantities that are arranged in different and judiciously chosen locations on the staggered mesh. The discrete pressure field at time  $t^n$  is denoted by  $p^{h,n}$  and its degrees of freedom are located in the center of each control volume as  $p^{p,q,n} = p(x^p, y^q, t^n)$ . Throughout this paper we denote with the superscript  $h$  the set of all degrees of freedom of the discrete solution and all degrees of freedom generated by a discrete operator, in order to ease the notation. The discrete velocities  $v_1^{h,n}$  and  $v_2^{h,n}$  are arranged in an edge-based staggered fashion, i.e.  $u^{p+\frac{1}{2},q,n} := v_1^{p+\frac{1}{2},q,n} = v_1(x^{p+\frac{1}{2}}, y^q, t^n)$  and  $v^{p,q+\frac{1}{2},n} := v_2^{p,q+\frac{1}{2},n} = v_2(x^p, y^{q+\frac{1}{2}}, t^n)$ . The discrete distortion field  $\mathbf{A}^{h,n}$  is defined on the *vertices* of each spatial control volume as  $A_{ik}^{p+\frac{1}{2},q+\frac{1}{2},n} = A_{ik}(x^{p+\frac{1}{2}}, y^{q+\frac{1}{2}}, t^n)$ . For clarity, see again Fig. 1.

The *discrete divergence operator*,  $\nabla^h \cdot$ , acting on a discrete vector field  $\mathbf{v}^{h,n}$  is abbreviated by  $\nabla^h \cdot \mathbf{v}^{h,n}$  and its degrees of freedom are given by

$$\nabla^{p,q} \cdot \mathbf{v}^{h,n} = \frac{u^{p+\frac{1}{2},q,n} - u^{p-\frac{1}{2},q,n}}{\Delta x} + \frac{v^{p,q+\frac{1}{2},n} - v^{p,q-\frac{1}{2},n}}{\Delta y}, \quad (31)$$

i.e. it is based on the *edge-based* staggered values of the field  $\mathbf{v}^{h,n}$ . It defines a discrete divergence on the control volume  $\Omega^{p,q}$  via the Gauss theorem,

$$\nabla^{p,q} \cdot \mathbf{v}^{h,n} = \frac{1}{\Delta x \Delta y} \int_{\Omega^{p,q}} \nabla \cdot \mathbf{v} d\mathbf{x} = \frac{1}{\Delta x \Delta y} \int_{\partial \Omega^{p,q}} \mathbf{v} \cdot \mathbf{n} dS, \quad (32)$$

based on the mid-point rule for the computation of the integrals along each edge of  $\Omega^{p,q}$ . In (32) the outward pointing unit normal vector to the boundary  $\partial \Omega^{p,q}$  of  $\Omega^{p,q}$  is denoted by  $\mathbf{n}$ . In a similar manner, the  $z$  component

of the *discrete curl*,  $\nabla^h \times$ , of a discrete vector field  $\mathbf{v}^{h,n}$  is denoted by  $(\nabla^h \times \mathbf{v}^{h,n}) \cdot \mathbf{e}_z$  and its degrees of freedom are naturally defined as

$$\begin{aligned} (\nabla^{p,q} \times \mathbf{v}^{h,n}) \cdot \mathbf{e}_z &= \varepsilon_{3jk} \partial_j^{p,q} v_k^{h,n} \\ &= \frac{1}{2} \left( \frac{v^{p+\frac{1}{2},q+\frac{1}{2},n} - v^{p-\frac{1}{2},q+\frac{1}{2},n}}{\Delta x} + \frac{v^{p+\frac{1}{2},q-\frac{1}{2},n} - v^{p-\frac{1}{2},q-\frac{1}{2},n}}{\Delta x} \right) \\ &\quad - \frac{1}{2} \left( \frac{u^{p+\frac{1}{2},q+\frac{1}{2},n} - u^{p+\frac{1}{2},q-\frac{1}{2},n}}{\Delta y} + \frac{u^{p-\frac{1}{2},q+\frac{1}{2},n} - u^{p-\frac{1}{2},q-\frac{1}{2},n}}{\Delta y} \right), \end{aligned} \quad (33)$$

making use of the *vertex-based* staggered values of the field  $\mathbf{v}^{h,n}$ , see the right panel in Fig. 2. In Eqn. (33) the symbol  $\varepsilon_{ijk}$  is again the usual Levi-Civita tensor. Eqn. (33) defines a discrete curl on the control volume  $\Omega^{p,q}$  via the Stokes theorem

$$(\nabla^h \times \mathbf{v}^{h,n}) \cdot \mathbf{e}_z = \frac{1}{\Delta x \Delta y} \int_{\Omega^{p,q}} (\nabla \times \mathbf{v}) \cdot \mathbf{e}_z \, d\mathbf{x} = \frac{1}{\Delta x \Delta y} \int_{\partial \Omega^{p,q}} \mathbf{v} \cdot \mathbf{t} \, dS, \quad (34)$$

based on the trapezoidal rule for the computation of the integrals along each edge of  $\Omega^{p,q}$  (here,  $\mathbf{t}$  stands for the tangent vector to the face of the control volume). Since the distortion field  $\mathbf{A}$  transforms as a vector and not as a rank 2 tensor ( $\mathbf{A}$  is a triad and thus a set of three vectors), the degrees of freedom of the  $z$ -component of the discrete curl of  $\mathbf{A}^{h,n}$  simply read

$$\begin{aligned} ((\nabla^{p,q} \times \mathbf{A}^{h,n}) \cdot \mathbf{e}_z)_i &= \varepsilon_{3jk} \partial_j^{p,q} A_{ik}^{h,n} \\ &= \frac{1}{2} \left( \frac{A_{i2}^{p+\frac{1}{2},q+\frac{1}{2},n} - A_{i2}^{p-\frac{1}{2},q+\frac{1}{2},n}}{\Delta x} + \frac{A_{i2}^{p+\frac{1}{2},q-\frac{1}{2},n} - A_{i2}^{p-\frac{1}{2},q-\frac{1}{2},n}}{\Delta x} \right) \\ &\quad - \frac{1}{2} \left( \frac{A_{i1}^{p+\frac{1}{2},q+\frac{1}{2},n} - A_{i1}^{p+\frac{1}{2},q-\frac{1}{2},n}}{\Delta y} + \frac{A_{i1}^{p-\frac{1}{2},q+\frac{1}{2},n} - A_{i1}^{p-\frac{1}{2},q-\frac{1}{2},n}}{\Delta y} \right). \end{aligned} \quad (35)$$

Last but not least, we need to define a discrete gradient operator that is compatible with the discrete curl, so that the continuous identity

$$\nabla \times \nabla \phi = 0 \quad (36)$$

also holds on the discrete level. If we define a scalar field in the barycenters of the control volumes  $\Omega^{p,q}$  as  $\phi^{p,q,n} = \phi(x^p, y^q, t^n)$  then the corner gradient generates a natural discrete gradient operator  $\nabla^h$  of the discrete scalar field  $\phi^{h,n}$  that defines a discrete gradient in all vertices of the mesh. The corresponding degrees of freedom generated by  $\nabla^h \phi^{h,n}$  read (see the left panel of Fig. 2)

$$\nabla^{p+\frac{1}{2},q+\frac{1}{2}} \phi^{h,n} = \partial_k^{p+\frac{1}{2},q+\frac{1}{2}} \phi^{h,n} = \begin{pmatrix} \frac{1}{2} \left( \frac{\phi^{p+1,q+1,n} - \phi^{p,q+1,n}}{\Delta x} + \frac{\phi^{p+1,q,n} - \phi^{p,q,n}}{\Delta x} \right) \\ \frac{1}{2} \left( \frac{\phi^{p+1,q+1,n} - \phi^{p+1,q,n}}{\Delta y} + \frac{\phi^{p,q+1,n} - \phi^{p,q,n}}{\Delta y} \right) \\ 0 \end{pmatrix}. \quad (37)$$

It is then straightforward to verify that an immediate consequence of (33) and (37) is

$$\nabla^h \times \nabla^h \phi^{h,n} = 0, \quad (38)$$

i.e. one obtains a discrete analogue of (36). We furthermore define the following averaging operators from the three different staggered meshes to the cell barycenter  $(x^p, y^q)$ :

$$\begin{aligned} A_{ik}^{p,q,n} &= \frac{1}{4} \left( A_{ik}^{p-\frac{1}{2},q-\frac{1}{2},n} + A_{ik}^{p+\frac{1}{2},q-\frac{1}{2},n} + A_{ik}^{p-\frac{1}{2},q+\frac{1}{2},n} + A_{ik}^{p+\frac{1}{2},q+\frac{1}{2},n} \right), \\ u^{p,q,n} &= \frac{1}{2} \left( u^{p-\frac{1}{2},q,n} + u^{p+\frac{1}{2},q,n} \right), \\ v^{p,q,n} &= \frac{1}{2} \left( v^{p,q-\frac{1}{2},n} + v^{p,q+\frac{1}{2},n} \right). \end{aligned} \quad (39)$$

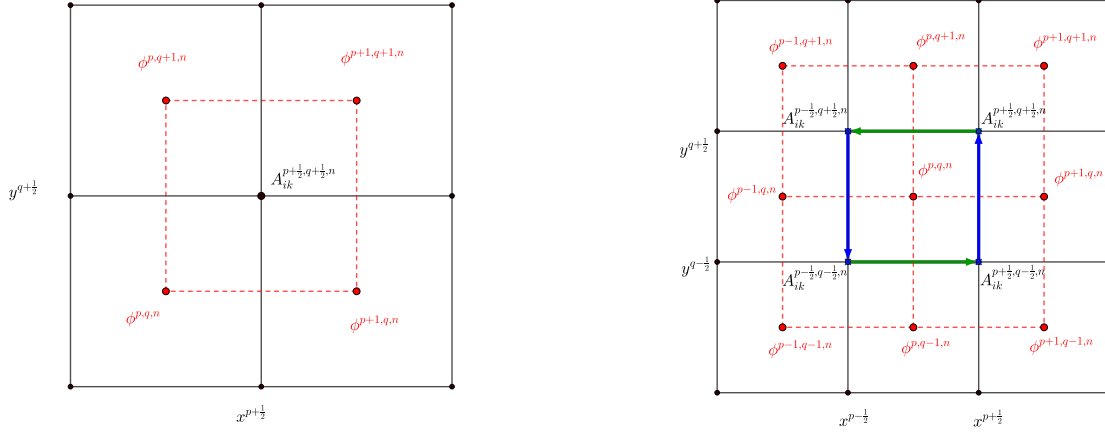


Figure 2: Left: stencil of the discrete gradient operator, which computes the corner gradient of a scalar field defined in the cell barycenter. Right: stencil of the discrete curl operator, which defines the curl inside the cell barycenter using the vector field components defined in the corners of the primary control volume. In the right panel we also show the total 9-point stencil that is needed for the discrete identity  $\nabla^h \times \nabla^h \phi^{h,n} = 0$ .

### 3.4. Explicit, curl-free compatible discretization of the distortion field

The key ingredient of the numerical method [13] is the proper discretization of the thermal impulse equation and of the PDE for the distortion field. We employ the following compatible discretization

$$\begin{aligned}
A_{ik}^{p+\frac{1}{2},q+\frac{1}{2},n+1} &= A_{ik}^{p+\frac{1}{2},q+\frac{1}{2},n} - \Delta t \partial_k^{p+\frac{1}{2},q+\frac{1}{2}} \left( A_{im}^{h,n} v_m^{h,n} \right) \\
&- \Delta t \frac{1}{4} \sum_{r=0}^1 \sum_{s=0}^1 v_m^{p+r,q+s,n} \left( \partial_m^{p+r,q+s} A_{ik}^{h,n} - \partial_k^{p+r,q+s} A_{im}^{h,n} \right) \\
&- \Delta t \frac{|\det(\mathbf{A})^{p+\frac{1}{2},q+\frac{1}{2},n+1}|^{\frac{5}{3}}}{\tau} A_{ij}^{p+\frac{1}{2},q+\frac{1}{2},n+1} G_{jk}^{p+\frac{1}{2},q+\frac{1}{2},n+1}.
\end{aligned} \tag{40}$$

It is easy to check that in the homogeneous case (when  $\tau \rightarrow \infty$  and therefore the algebraic source term vanishes) for an initially curl-free vector field  $\mathbf{A}^{h,n}$  that satisfies  $\nabla^h \times \mathbf{A}^{h,n} = 0$  also  $\nabla^h \times \mathbf{A}^{h,n+1} = 0$  holds. To see this, one needs to apply the discrete curl operator  $\nabla^h \times$  to (40). One realizes that the second row of (40), which contains the discrete curl of  $\mathbf{A}^{h,n}$  vanishes immediately, due to  $\nabla^h \times \mathbf{A}^{h,n} = 0$ . The third row vanishes because  $\tau \rightarrow \infty$ . The curl of the first term on the right hand side in the first row of (40) is zero because of  $\nabla^h \times \mathbf{A}^{h,n} = 0$  and the curl of the second term is zero because of  $\nabla^h \times \nabla^h \phi^{h,n} = 0$ , with the auxiliary scalar field  $\phi^{h,n} = A_{im}^{h,n} v_m^{h,n}$ , whose degrees of freedom are computed as  $\phi^{p,q,n} = A_{im}^{p,q,n} v_m^{p,q,n}$  after averaging of the velocity vector and the distortion into the barycenters of the control volumes  $\Omega^{p,q}$ . Note that on uniform grids this average is second order accurate.

### 3.5. Implicit solution of the pressure equation

Up to now, the contribution of the pressure to the momentum and to the total energy conservation laws, i.e. the terms contained in the pressure fluxes  $\mathbf{F}_p$ , have been excluded. The discrete momentum equations including the pressure terms read (recall that  $u = v_1$  and  $v = v_2$ )

$$\begin{aligned}
(\rho u)^{p+\frac{1}{2},q,n+1} &= (\rho u)^{p+\frac{1}{2},q,*} - \frac{\Delta t}{\Delta x} (p^{p+1,q,n+1} - p^{p,q,n+1}), \\
(\rho v)^{p,q+\frac{1}{2},n+1} &= (\rho v)^{p,q+\frac{1}{2},*} - \frac{\Delta t}{\Delta y} (p^{p,q+1,n+1} - p^{p,q,n+1}),
\end{aligned} \tag{41}$$

where pressure is taken *implicitly*, while all nonlinear convective terms and the vertex fluxes have already been discretized *explicitly* via the operators  $(\rho u)^{p+\frac{1}{2},q,*}$  and  $(\rho v)^{p,q+\frac{1}{2},*}$  given in (27) and after averaging of the obtained

quantities back to the edge-based staggered dual grid. Recalling that  $E_i(\rho, p)$ ,  $E_e(A_{ik})$ , and  $E_k(v_k)$  are three contributions to the specific total energy  $E$  given by (3), a preliminary form of the discrete total energy equation reads

$$\begin{aligned} \rho E_i(p^{p,q,n+1}) + \rho E_e^{p,q,n+1} + \rho \tilde{E}_k^{p,q,n+1} &= \rho E^{p,q,*} \\ &- \frac{\Delta t}{\Delta x} \left( \tilde{h}^{p+\frac{1}{2},q,n+1} (\rho u)^{p+\frac{1}{2},q,n+1} - \tilde{h}^{p-\frac{1}{2},q,n+1} (\rho u)^{p-\frac{1}{2},q,n+1} \right) \\ &- \frac{\Delta t}{\Delta y} \left( \tilde{h}^{p,q+\frac{1}{2},n+1} (\rho v)^{p,q+\frac{1}{2},n+1} - \tilde{h}^{p,q-\frac{1}{2},n+1} (\rho v)^{p,q-\frac{1}{2},n+1} \right). \end{aligned} \quad (42)$$

Here, we have used the abbreviation  $\rho E_i(p^{p,q,n+1}) = \rho^{p,q,n+1} E_i(p^{p,q,n+1}, \rho^{p,q,n+1})$ . Inserting the discrete momentum equations (41) into the discrete energy equation (42) and making tilde symbols explicit via a simple Picard iteration (using the lower index  $r$  in the following), as suggested in [28, 27], leads to the following discrete wave equation for the unknown pressure:

$$\begin{aligned} &\rho^{p,q,n+1} E_i(p_{r+1}^{p,q,n+1}, \rho^{p,q,n+1}) \\ &- \frac{\Delta t^2}{\Delta x^2} \left( h_r^{p+\frac{1}{2},q,n+1} \left( p_{r+1}^{p+1,j,n+1} - p_{r+1}^{p,q,n+1} \right) - h_r^{p-\frac{1}{2},q,n+1} \left( p_{r+1}^{p,q,n+1} - p_{r+1}^{p-1,q,n+1} \right) \right) \\ &- \frac{\Delta t^2}{\Delta y^2} \left( h_r^{p,q+\frac{1}{2},n+1} \left( p_{r+1}^{p,q+1,n+1} - p_{r+1}^{p,q,n+1} \right) - h_r^{p,q-\frac{1}{2},n+1} \left( p_{r+1}^{p,q,n+1} - p_{r+1}^{p,q-1,n+1} \right) \right) = b_r^{p,q,n}, \end{aligned} \quad (43)$$

with the known right hand side

$$\begin{aligned} b_r^{p,q,n} &= \rho E^{p,q,*} - \rho E_e^{p,q,n+1} - \rho E_{k,r}^{p,q,n+1} \\ &- \frac{\Delta t}{\Delta x} \left( h_r^{p+\frac{1}{2},q,n+1} (\rho u)^{p+\frac{1}{2},q,*} - h_r^{p-\frac{1}{2},q,n+1} (\rho u)^{p-\frac{1}{2},q,*} \right) \\ &- \frac{\Delta t}{\Delta y} \left( h_r^{p,q+\frac{1}{2},n+1} (\rho v)^{p,q+\frac{1}{2},*} - h_r^{p,q-\frac{1}{2},n+1} (\rho v)^{p,q-\frac{1}{2},*} \right). \end{aligned} \quad (44)$$

The density at the new time  $\rho^{p,q,n+1} = \rho^{p,q,*}$  is already known from (27), and also the energy contribution  $\rho E_e^{p,q,n+1}$  of the distortion field  $\mathbf{A}^{h,n+1}$  is already known, after averaging onto the main grid of the staggered field components that have been evolved in the vertices via the compatible discretization (40) and (40). The final system for the pressure (43) forms a *mildly nonlinear system* of the form

$$\rho \mathbf{E}_i(\mathbf{p}_{r+1}^{n+1}) + \mathbf{M}_r \cdot \mathbf{p}_{r+1}^{n+1} = \mathbf{b}_r^n \quad (45)$$

as in [28], with a linear part contained in  $\mathbf{M}_r$  that is symmetric and at least positive semi-definite. In one space dimension  $\mathbf{M}_r$  is tridiagonal, while it is pentadiagonal in two space dimensions. Hence, with the usual assumptions on the nonlinearity detailed in [25], it can be efficiently solved with the nested Newton method of Casulli and Zanolli [24, 25]. As already stated in [28] for equations of state whose dependence of the internal energy density is *linear* in the pressure, the system (45) reduces to a *linear* one. Only for more complex cubic or tabulated equations of state, (45) becomes nonlinear.

We further note that in the incompressible limit (i.e. when the Mach number tends to zero,  $\text{Ma} \rightarrow 0$ ), following the asymptotic analysis performed in [58, 59, 60, 63], the pressure tends to a constant and the contribution of the kinetic energy  $\rho E_k$  can be neglected w.r.t.  $\rho E_i$ . Therefore, in the incompressible limit the system (43) tends to the usual pressure Poisson equation of incompressible flow solvers. In each Picard iteration, after the solution of the pressure system (43), the enthalpies at the interfaces are recomputed and the momentum is updated by

$$(\rho u)_{r+1}^{p+\frac{1}{2},q,n+1} = (\rho u)^{p+\frac{1}{2},q,*} - \frac{\Delta t}{\Delta x} \left( p_{r+1}^{p+1,q,n+1} - p_{r+1}^{p,q,n+1} \right), \quad (46)$$

$$(\rho v)_{r+1}^{p,q+\frac{1}{2},n+1} = (\rho v)^{p,q+\frac{1}{2},*} - \frac{\Delta t}{\Delta y} \left( p_{r+1}^{p,q+1,n+1} - p_{r+1}^{p,q,n+1} \right), \quad (47)$$

from which the new kinetic energy density  $(\rho E)_{k,r+1}^{p,q,n+1}$  can be computed after averaging the momentum onto the main grid. At the end of the Picard iterations, the total energy is updated as

$$\begin{aligned}
(\rho E)^{p,q,n+1} = & (\rho E)^{p,q,*} - \frac{\Delta t}{\Delta x} \left( h^{p+\frac{1}{2},q,n+1} (\rho u)^{p+\frac{1}{2},q,n+1} - h^{p-\frac{1}{2},q,n+1} (\rho u)^{p-\frac{1}{2},q,n+1} \right) \\
& - \frac{\Delta t}{\Delta y} \left( h^{p,q+\frac{1}{2},n+1} (\rho v)^{p,q+\frac{1}{2},n+1} - h^{p,q-\frac{1}{2},n+1} (\rho v)^{p,q-\frac{1}{2},n+1} \right), \quad (48)
\end{aligned}$$

while the final momentum is averaged back onto the main grid. This completes the description of our new curl-free semi-implicit finite volume scheme for the GPR model of continuum mechanics in the two-dimensional case recently proposed in [13]. Due to the *operator splitting* between the explicit subsystem and the implicit pressure system and due to the fully implicit treatment of the algebraic source terms (backward Euler), the scheme proposed in this paper is globally only first order accurate in time. To obtain higher order in time, an IMEX Runge-Kutta scheme should be used, see [64, 65, 11, 12].

## 4. Numerical results

Throughout this section, we use the notations  $u = v_1$ ,  $v = v_2$  for the velocity components, and  $x = x_1$ ,  $y = x_2$  for the coordinates. In all the presented test cases, the CFL number for the explicit step of SISPFV scheme was set to 0.95 and was chosen based on the shear sound speed  $c_{sh}$  which was set to 10 or higher and thus, greater than the flow velocity which was typically of the order of 1.

### 4.1. Couette flow

In the first example, we verify the model in the standard Couette flow problem with ( $\sigma_Y > 0$ ) and without ( $\sigma_Y = 0$ ) the yield stress. The two-dimensional computational domain  $(x, y) \in [0, 1] \times [0, 1]$  has periodic boundary conditions in  $x$ -direction, and no-slip conditions at  $y = 0$  and  $y = 1$ . Additionally, the boundary  $y = 1$  is moving in the positive direction at a constant velocity. We solve system (2) with the SISPFV scheme [13] on a grid composed of  $4 \times 100$  elements until time  $t = 10$  for a range of velocities of the moving boundary. At time  $t = 10$ , the velocity  $u(y)$  has already reached a constant slope while the stress  $\sigma_{12}(y)$  is constant (symbols in Fig. 3). The initial conditions are set to  $\rho = 1$ ,  $\mathbf{A} = \mathbf{I}$ ,  $\mathbf{v} = 0$ . The material parameters of the GPR model are  $c_{sh} = 10$ , while the relaxation time  $\tau$  is defined from the Herschel-Bulkley viscosity which has the parameters  $\sigma_Y = 0$  or  $\sigma_Y = 0.5$ ,  $\kappa = 1$ ,  $n = 0.5, 1.0$ , or 1.5. The relaxation time in the solid state is taken as  $\tau_s = 10^{10}$ , while the fluid state relaxation time is computed from (18). In Fig. 3, one can notice that the yield-stress and power-law rheology of the HB model is well captured by the GPR model.

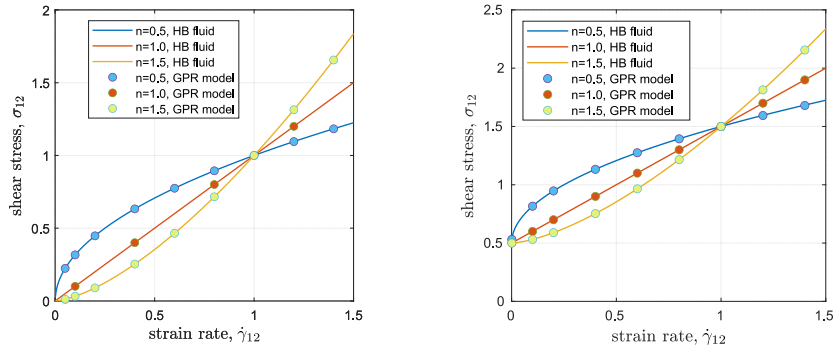


Figure 3: Couette flow. Comparison of the numerical solution to the GPR model obtained with the SPSIFV scheme (symbols) versus the analytical solution of the HB model for a range of  $\dot{\gamma}_{12}$ , and for  $\sigma_Y = 0$  (left, no yield stress) and  $\sigma_Y = 0.5$  (right). Other material parameters are  $\kappa = 1.0$ ,  $n = 0.5$ ,  $n = 1.0$ , and  $n = 1.5$ . The parameters of the GPR model are  $c_{sh} = 10$ ,  $\tau_s = 10^{10}$ .

We also use the Couette flow example to demonstrate a peculiar feature of the distortion field. Namely, its intrinsic rotational dynamics. Recall that the distortion  $\mathbf{A}$  can be viewed as a local frame field (local basis triad) consisting of three linearly independent vectors. As has been noticed earlier [71, 31], the relaxation process in  $\mathbf{A}$  governed by the right-hand side in (2c) acts in such a way that the tangential stresses tend to reduce but also the basis triad  $\mathbf{A}$  rotates permanently even in the case when the velocity field is stationary. In the current formulation, the distortion spin does not affect the stress tensor  $\boldsymbol{\sigma}$ , e.g. see [46], and does not violate the angular momentum conservation because the stress  $\boldsymbol{\sigma}$  stays always symmetric. An extension of the model towards accounting for the distortion spin and associating it to, for example, unresolved small-scale eddies in turbulent flows is discussed in [72] in the context of the Riemann-Cartan geometry.

Fig. 4 shows strong heterogeneity in the distortion field due to the intrinsic rotations despite the velocity and the stress are homogeneous and steady. In this regards, one may recall the polar decomposition for the distortion matrix  $\mathbf{A} = \mathbf{R}\sqrt{\mathbf{G}}$ , with  $\mathbf{R}$  being an orthonormal matrix, and the fact that the stress  $\boldsymbol{\sigma}$  (5) does not depend on the rotation  $\mathbf{R}$ , see [46]. To demonstrate this feature of the model, we carried out three simulations of the Couette flow in the domain  $(x, y) \in [0, 1] \times [0, 1]$  with the GPR model and SISPFV scheme of a Newtonian fluid with  $\eta = 10^{-1}$ ,  $\eta = 10^{-2}$ , and  $\eta = 10^{-3}$ , see Fig. 4. The numerical solutions are shown at times approximately right after the steady state is reached,  $t = 5$  for  $\eta = 10^{-1}$ ,  $t = 50$  for  $\eta = 10^{-2}$ , and  $t = 500$  for  $\eta = 10^{-3}$ . Initially, the fluid is at rest with the parameters  $\rho = 1$ ,  $\mathbf{v} = 0$ ,  $\mathbf{A} = \mathbf{I}$  and  $c_{\text{sh}} = 10$ . The velocity of the moving boundary ( $y = 1$ ) is set to 1. A mesh of  $4 \times 400$  elements was used for  $\eta = 10^{-1}$  and  $10^{-2}$ , while to resolve the strong heterogeneity of  $\mathbf{A}$  at  $\eta = 10^{-3}$  we were need to use a quite fine mesh of  $4 \times 1600$  elements. A slight deviation from the constant value in  $\sigma_{12}$  is visible for the case  $\eta = 10^{-3}$  (bottom) which is due to the fact that at this mesh resolution and with the second-order accuracy of our SISPFV scheme we are still not able to resolve high heterogeneity of the distortion field in the interval  $y \in [0.8, 1]$  of the most intense heterogeneity of  $\mathbf{A}$ . Remark that the actual deformation of the fluid elements which is stored in  $\mathbf{G}$  are of the order of  $10^{-3}$  while the elements of the rotation matrix  $\mathbf{R}$  are of the order of 1. Therefore, one may conclude that for high Reynolds number, the lack of the resolution of rotational peculiarities of the distortion field might result in errors in the stress tensor.

#### 4.2. Plane Hagen-Poiseuille flow

In the second numerical example, we test the GPR model in the plane Hagen-Poiseuille flow. The two-dimensional computational domain  $(x, y) \in [0, 1] \times [0, 1]$  has periodic boundary conditions in  $x$ -direction, and no-slip conditions at  $y = 0$  and  $y = 1$ . We solve system (2) with the SISPFV scheme on a grid composed of  $4 \times 100$  elements. The pressure drop  $\Delta p$  is set to 0.1. In the initial conditions, we set the material velocity equal to the analytical solution (49), and other state variables were set as  $\rho = 1$ ,  $\mathbf{A} = \mathbf{I}$ . The final integration time is  $t = 1$ . The analytical solution to the HB model is given by (e.g. see [7])

$$u(y) = \begin{cases} \frac{1}{m} f \left( \left( \frac{y_0}{h} \right)^m - \left( \frac{y_0 - y}{h} \right)^m \right), & y \leq y_0, \\ \frac{1}{m} f \left( \frac{y_0}{h} \right)^m, & y_0 \leq y \leq h - y_0, \\ \frac{1}{m} f \left( \left( \frac{y_0}{h} \right)^m - \left( \frac{y - (h - y_0)}{h} \right)^m \right), & y > h - y_0, \end{cases} \quad (49)$$

where  $f = \frac{h}{V} \left( \frac{\Delta p h}{\kappa} \right)^{1/n}$ ,  $m = 1 + 1/n$ ,  $y_0 = h(1/2 - \text{Bi}/f^n)$ ,  $h$  is the channel width,  $V$  is a velocity scale, and  $\text{Bi}$  is the generalized Bingham number which for the HB model can be defined as

$$\text{Bi} = \frac{\sigma_Y}{\kappa} \left( \frac{h}{V} \right)^n 2^{1-n}, \quad (50)$$

and which quantifies the effect of yield stress versus power-law, e.g. [79]. In the examples of this section, we set  $h = 1.0$  (dimension in the  $y$ -direction) and we set the velocity scale  $V = 1$  for  $n = 1$  and  $V = 2.03$  for  $n \neq 1$ .

Fig. 5 depicts the numerical solution to the GPR model and the analytical solution (49) to the HB model for a range of power-law exponents  $n = 0.5, 1.0$ , and  $1.5$  and zero yield-stress  $\sigma_Y = 0$  ( $\text{Bi} = 0$ ). The consistency index was taken as  $\kappa = 1.0$ . The shear sound speed in the GPR model was taken as  $c_{\text{sh}} = 10$ . The relaxation time in



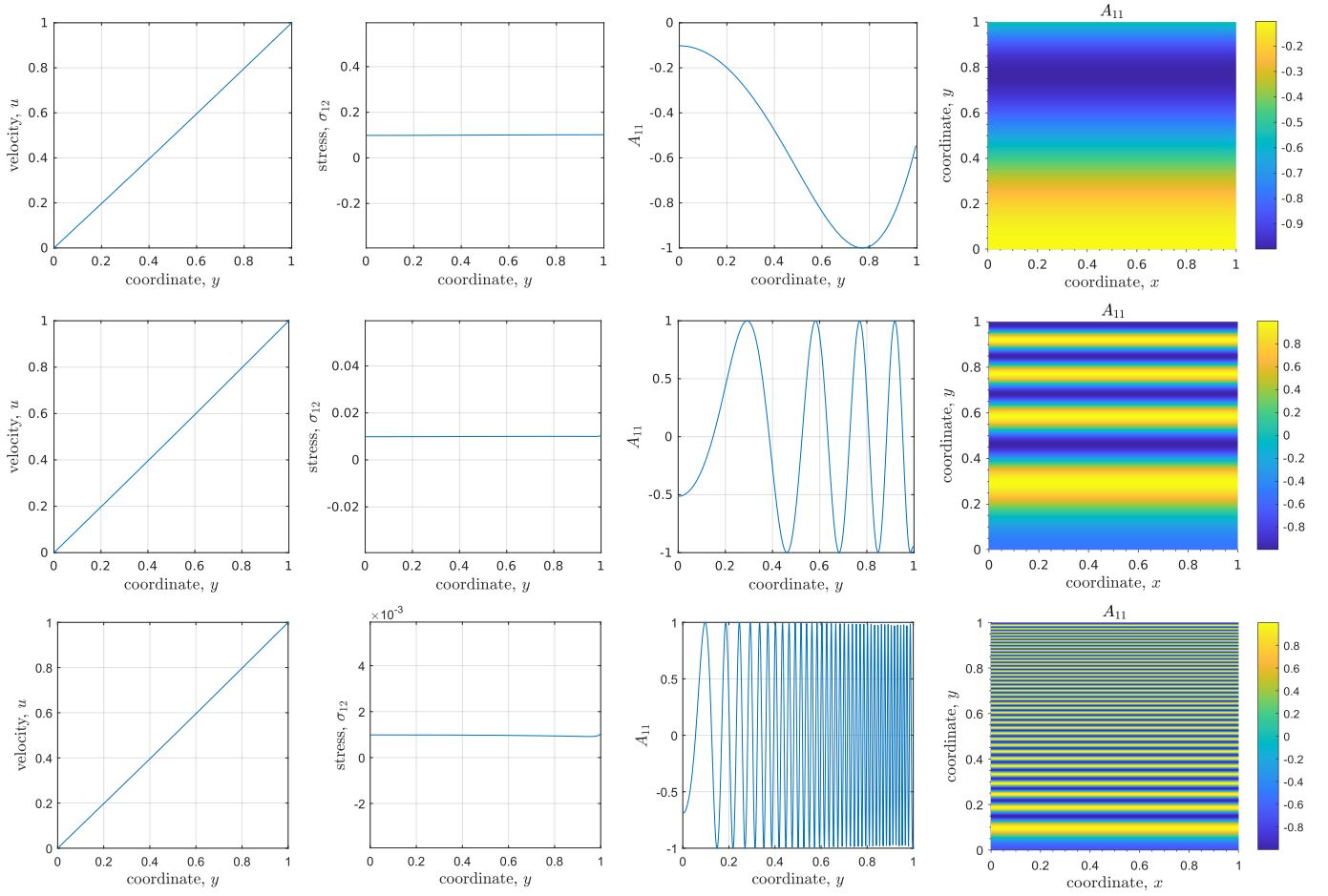


Figure 4: Couette flow of a Newtonian fluid obtained with our model for the Newtonian viscosity  $\eta = 10^{-1}$  (top row, final time  $t = 5$ ),  $\eta = 10^{-2}$  (middle row, final time  $t = 50$ ), and  $\eta = 10^{-3}$  (bottom, final time  $t = 500$ ). Cuts of the velocity  $u$ , stress  $\sigma_{12}$ , and  $A_{11}$  component of the distortion, as well as a snapshot of  $A_{11}$  (right column). The third and fourth columns demonstrate different orientations of the distortion field of the fluid layers due to the intrinsic rotations. The higher the Reynolds number the higher the orientational heterogeneity in the distortion field.

the solid state is taken as  $\tau_s = 10^{20}$ , while the fluid state relaxation time is computed from (18). Overall, a good agreement between the solutions is achieved.

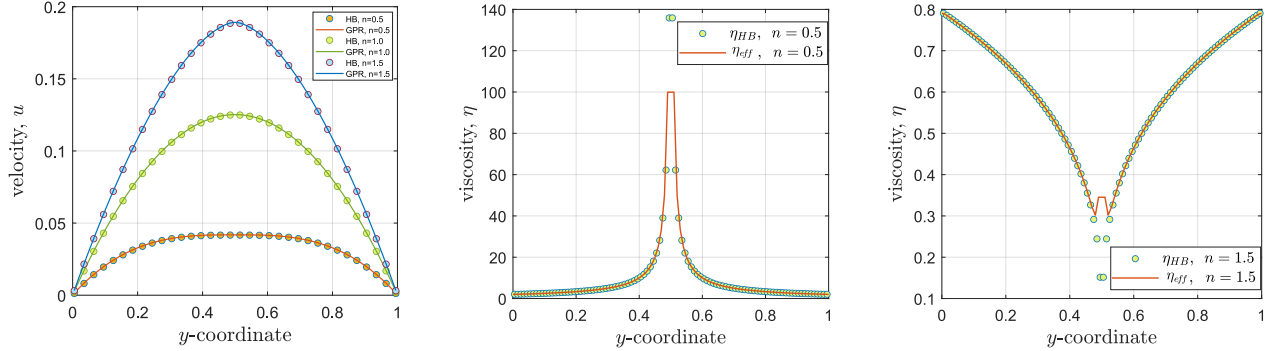


Figure 5: Hagen-Poiseuille flow. Comparison of the numerical solution to the GPR model obtained with the SISPFV scheme against the analytical solution to the Herschel-Bulkley model ( $\sigma_Y = 0$ ) for the power-law exponents  $n = 0.5$ ,  $n = 1.0$ , and  $n = 1.5$  (left subfigure, from bottom to top). The middle and right subfigures show the effective viscosity of the GPR model  $\eta_{eff} = \frac{1}{6}\rho\tau c_{sh}^2$  (lines) and the HB viscosity (symbols) computed from the analytical solution (49).

Fig. 6 (left subfigure) shows the numerical solution to the GPR model for a range Bingham numbers  $Bi = 0.0, 0.1, 0.2, 0.3, 0.4$ , and  $0.5$  and power-law index  $n = 1$ . A good agreement between the GPR solution and the solution to the HB model is achieved. The middle subfigure of Fig. 6 also shows a typical behavior of the relaxation time  $\tau(\mathbf{A})$ . The numerical solution for the same range of Bingham numbers but the power-law index  $n = 0.5$  is shown in Fig. 6 (right subfigure). Also, a good agreement between the solution of our hyperbolic model and the parabolic model is achieved.

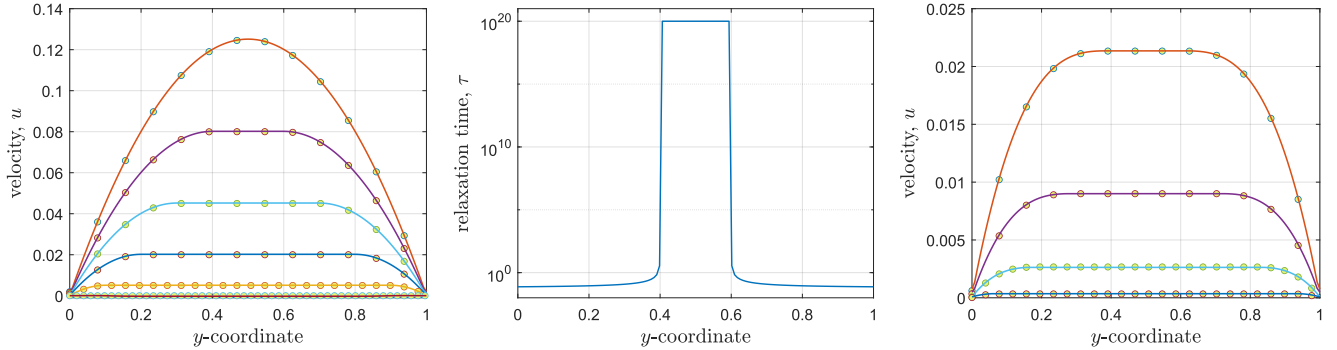


Figure 6: Hagen-Poiseuille flow of Herschel-Bulkley fluid for  $n = 1.0$  (left) and  $n = 0.5$  (right). Comparison of the numerical solution  $u(y)$  to the GPR model (lines) against the analytical solution (49) to the HB model (symbols) for the range of Bi numbers:  $Bi = 0, 0.1, 0.2, 0.3, 0.4$ , and  $0.5$  (from top to bottom) for  $n = 1.0$  and  $Bi = 0.1, 0.2, 0.3$ , and  $0.4$  for  $n = 0.5$ . The middle subfigure shows a typical behavior of the relaxation time ( $n = 1.0$ ,  $Bi = 0.1$ ).

### 4.3. Lid-driven cavity flow

In the third example, we consider another classical benchmark problem for the numerical solution of incompressible Navier-Stokes equations, the lid-driven cavity problem. As previously, we compute the numerical solution to the GPR model with the SISPFV scheme and it with the numerical solutions [79, 80] to the Herschel-Bulkley model for the both cases  $\sigma_Y = 0$  and  $\sigma_Y > 0$ .

### 4.3.1. Power-law fluid

For the computational setup in this section, the computational domain is given by  $[0, 1] \times [0, 1]$ . The initial condition is simply given by  $\rho = 1$ ,  $\mathbf{v} = 0$ , and  $\mathbf{A} = \mathbf{I}$ . The shear sound speed was set to  $c_{\text{sh}} = 10$ . The lid velocity ( $y = 1$ ) was set to 1 and no-slip boundary condition is imposed on the other boundaries. The parameters of the Herschel-Bulkley model are  $\kappa = 10^{-2}$ ,  $n = 0.5, 1.0, 1.5$ , and also in this section,  $\sigma_Y = 0$ . The Reynolds number estimated based on the consistency index  $\kappa$  is  $\text{Re} = 100$ . The computational domain was discretized with  $256 \times 256$  elements for  $n = 1.0$  and  $n = 1.5$  but we had to use a very fine mesh of  $1600 \times 1600$  elements in the most difficult for us case  $n = 0.5$ . This is conditioned by the fact that for  $n = 0.5$ , locally, the relaxation time drops down to  $10^{-5}$  and below which results in a very stiff source term in (2c). To efficiently deal with such a stiffness in the source term it is necessary to have an asymptotic preserving scheme while we recall that our SISPFV scheme is only quasi asymptotic-preserving property, see Section 3 and [13].

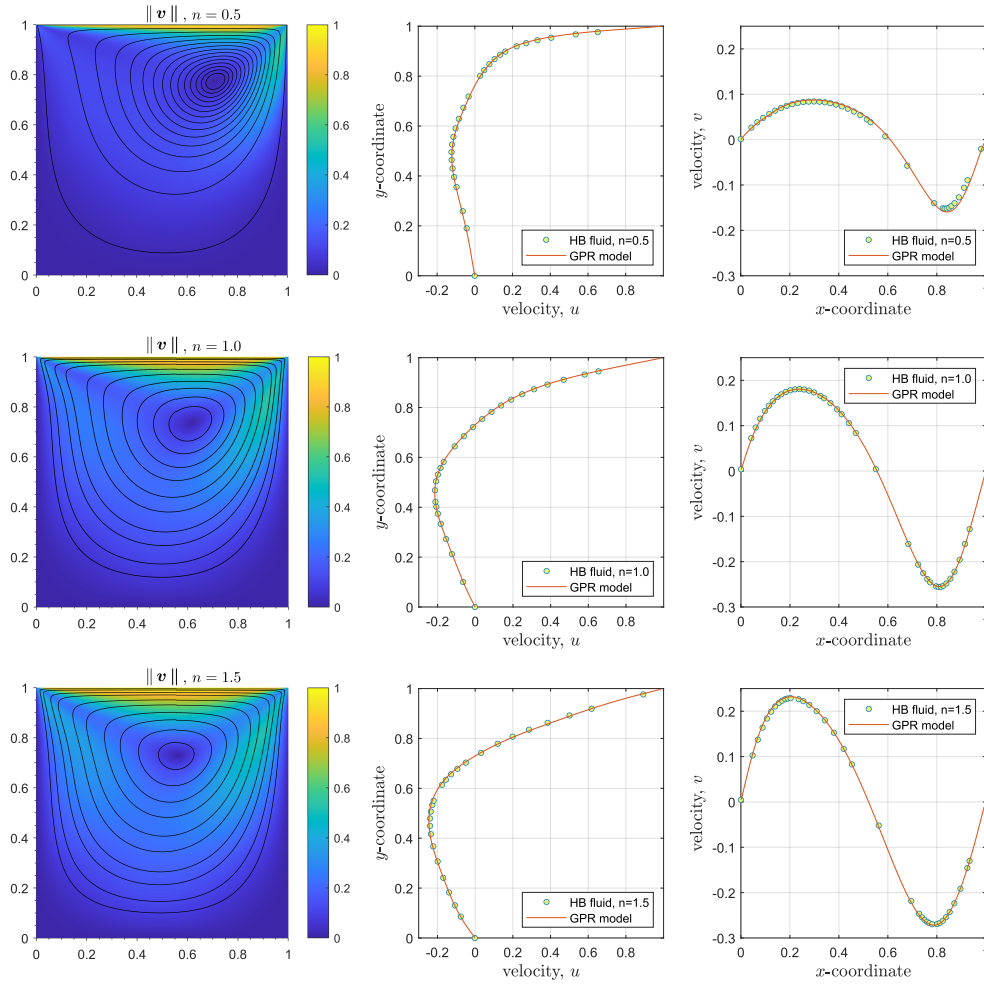


Figure 7: Lid-driven cavity flow, for the GPR model with the power-law exponents  $n = 0.5$  (top row,  $t = 30$ ),  $n = 1.0$  (middle row,  $t = 20$ ), and  $n = 1.5$  (bottom row,  $t = 20$ ) and  $c_{\text{sh}} = 10$ . Middle and right column shows the cuts of the velocity field in  $x = 0.5$  and  $y = 0.5$  (red lines) and reference numerical solution (symbols) from [79] obtained with the Herschel-Bulkley model for  $\kappa = 10^{-2}$ , zero yield stress, and the same power-law exponents  $n = 0.5, 1.0$ , and  $1.5$ .

Fig. 7 shows the snapshots of  $\|\mathbf{v}\|$  alongside with the streamlines and the cuts  $u(y)$  and  $v(x)$  of the velocity field at  $x = 0.5$  and  $y = 0.5$ , accordingly. Overall, one can notice a good agreement between the numerical solution

obtained with the SISPFV scheme for the first-order hyperbolic GPR model and the reference solution [79] to the parabolic Navier-Stokes equations with the Herschel-Bulkley viscosity.

Because the velocity fields depicted in Fig. 7 agree well with the reference solution of the Navier-Stokes equations with the Herschel-Bulkley viscosity, we can use this velocity data in order to compute the Navier-Stokes stress tensor (11) and compare it with the stress tensor of the GPR model computed from the distortion field according to (5). Note that the Navier-Stokes  $\sigma_{NS}$  (11) and the stress of the GPR model  $\sigma$  (5) are of different nature. The Navier-Stokes stress is of dissipative nature and is non-local (depends on the spatial gradient of the state variables) while  $\sigma$  is of elastic nature (non-dissipative) and computed locally (no space derivatives of state variables). Nevertheless, one can see in Fig. 8 that the two agree reasonably well.

Finally, Fig. 9 and Fig. 10 show non-trivial dynamics of the distortion field. We plot only  $A_{11}$  component but the others have a similar distribution. The real deformations of the material elements are tiny and contained in the metric tensor  $\mathbf{G} = \mathbf{A}^\top \mathbf{A}$  and they are hidden beyond the rotations  $\mathbf{R}$  (see the discussion to Fig. 4 in Section 4.1) whose elements vary between  $-1$  and  $1$ . Also, note that the dynamics of  $\mathbf{A}$  is never steady even if other quantities (density, velocity) reach the steady-state. Thus, the colors in Fig. 9 and Fig. 10 keep evolving in time while preserving the overall pattern.

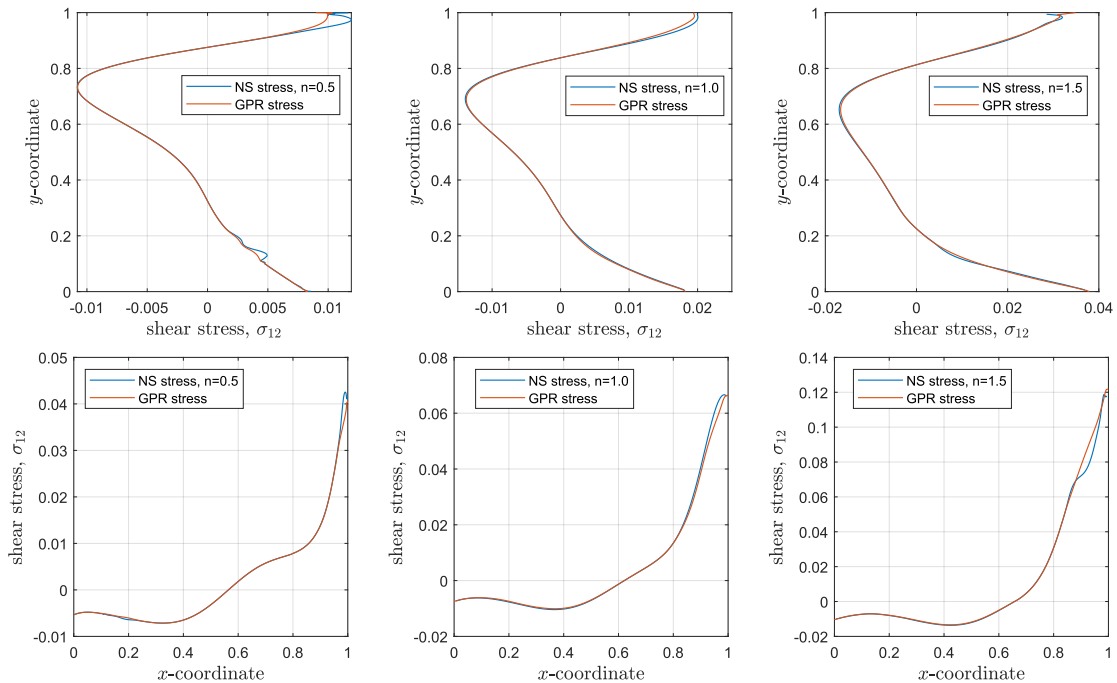


Figure 8: Lid-driven cavity flow. Comparison of the Navier-Stokes stress  $\sigma_{NS} = \eta(\dot{\gamma})\dot{\gamma}$  (computed from the velocity gradient of the GPR solution as a post-processing) and the stress of the GPR model computed from the distortion field  $\sigma = -\rho \mathbf{A}^\top \mathbf{E} \mathbf{A}$ . Despite an overall good agreement being achieved some deviations are also visible which are due to the fact that our scheme is not perfectly asymptotic preserving but only quasi-asymptotic preserving.

#### 4.4. Viscoplastic fluids

In the last numerical example, we run the simulation of the lid-driven cavity flow of our model in the elastoviscoplastic regime, i.e. with  $\sigma_Y > 0$ . In this example, we only consider  $n = 1.0$  (i.e. the Herschel-Bulkley viscosity reduces to the Bingham viscosity). First, we run the model at Bingham numbers  $\text{Bi} = 1, 10, \text{ and } 100$  at low Reynolds number  $\text{Re} = 1$  and then at the same Bingham numbers but at Reynolds  $\text{Re} = 100$ . In all the simulation of this section, the yield stress  $\sigma_Y$  is computed from (50) with  $h = 1, V = 2.03$ . The lid velocity is set to 1 while

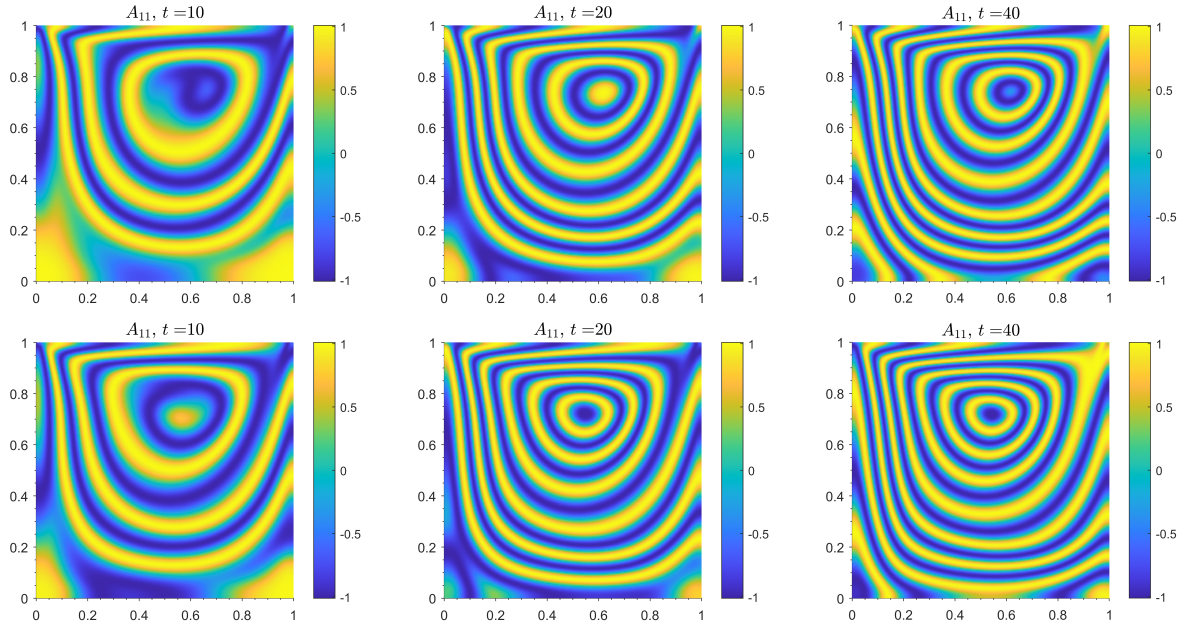


Figure 9: Snapshots of  $A_{11}$  for the lid-driven cavity flow of the GPR model with the power-law exponents  $n = 1.0$  (top row) and  $n = 1.5$  (bottom row) at times  $t = 10, 20,$  and  $40$ .

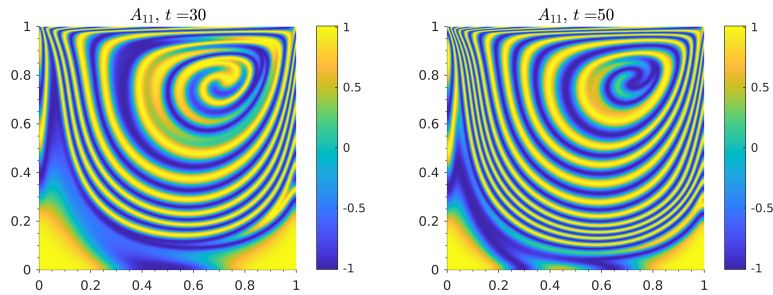


Figure 10: Snapshots of  $A_{11}$  for the lid-driven cavity flow of the GPR model with the power-law exponent  $n = 0.5$  at times  $t = 30$  and  $50$ .

the Reynolds number is controlled via setting  $\kappa = 1$  ( $Re = 1$ ) or  $\kappa = 10^{-2}$  ( $Re = 100$ ). Initially, the material is at rest with the parameters  $\rho = 1$ ,  $\mathbf{v} = 0$ ,  $\mathbf{A} = \mathbf{I}$ , while the simulation lasts until the velocity reaches the steady state.

Recall that the “softness” of the solid state in our model is characterized by the shear sound speed  $c_{sh}$  and because in the reference solution of the Bingham model we shall compare with, the solid state is treated as infinitely rigid we were need to take also a higher shear sound  $c_{sh}$  than in the previous examples. We chose  $c_{sh} = 50$  for all the simulations presented below.

Fig. 11 depicts the results at Reynolds number  $Re = 1$  and  $Bi = 1, 10, \text{ and } 100$ . We plot the snapshots of  $\sigma/\sigma_Y$  which can be used to distinguish the solidified ( $\sigma/\sigma_Y < 1$ ) and fluid ( $\sigma/\sigma_Y > 1$ ) regions. One can also use for that purpose the relaxation time  $\tau$  also depicted in Fig. 11. We can notice overall a good agreement with the reference solution reproduced from [80] and obtained with a steady state finite volume solver for the Bingham model. To compute the solution, a mesh of  $256^2$  cells was used for  $Bi = 1$  and  $Bi = 10$ , while the a mesh of  $512^2$  cells was used in the case of  $Bi = 100$ .

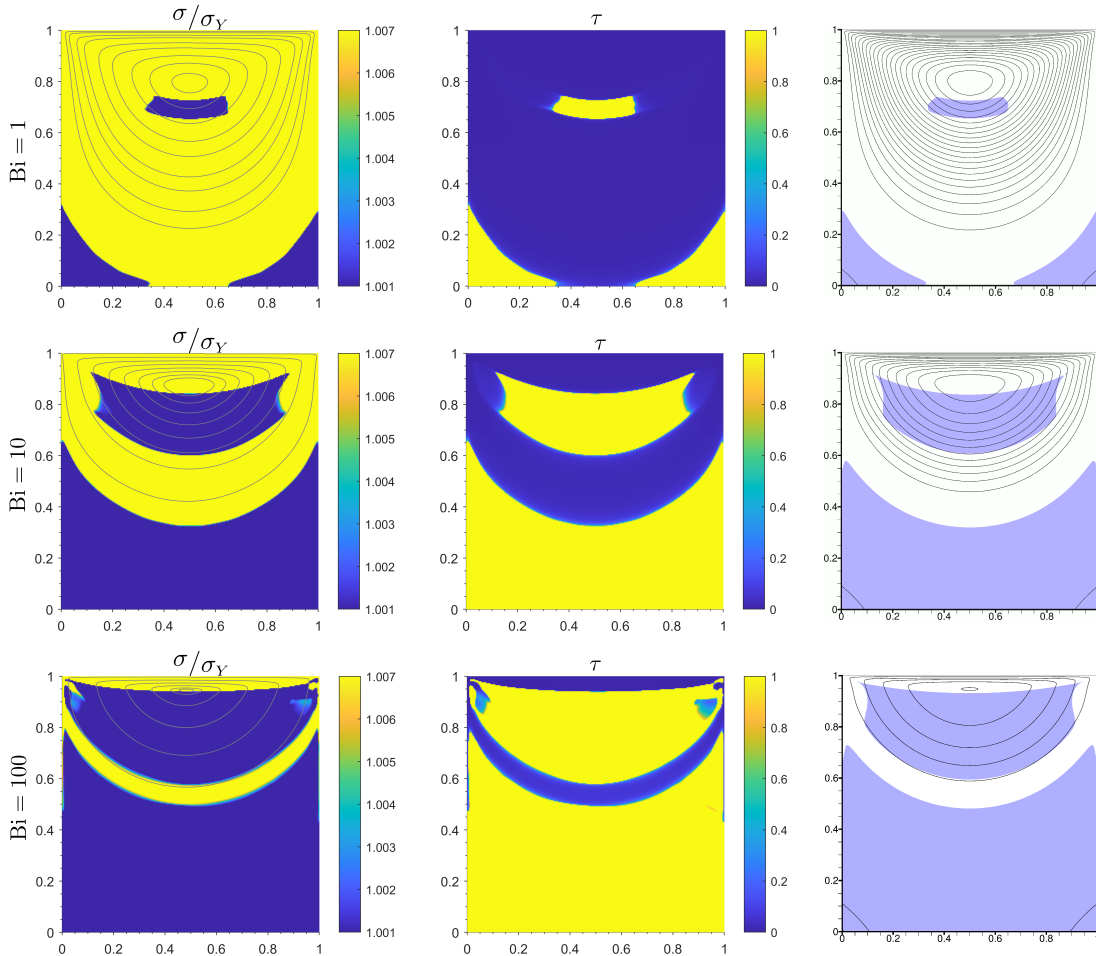


Figure 11: Lid-driven cavity flow of GPR model in the elastoviscoplastic regime at low Reynolds number  $Re = 1$  ( $\kappa = 1$ ) for  $Bi = 1$  (top row),  $Bi = 10$  (middle row), and  $Bi = 100$  (bottom row). The power-law exponent is set to  $n = 1.0$ . The equivalent stress (left column) can be used to visualize the unyielded regions (blue,  $\sigma/\sigma_Y > 1$ ). Second columns shows the relaxation time with the yellow color denoting the unyielded regions (for visualization, we color all cells with  $\tau > 1$  in yellow). The reference solution of the Bingham model (reproduced from [80]) is shown in the right column. The shaded regions denote the unyielded regions  $\sigma > \sigma_Y$ .

Finally, Fig. 12 and Fig. 13 show the solution to the GPR model at  $Re = 100$ . This time, we also have the

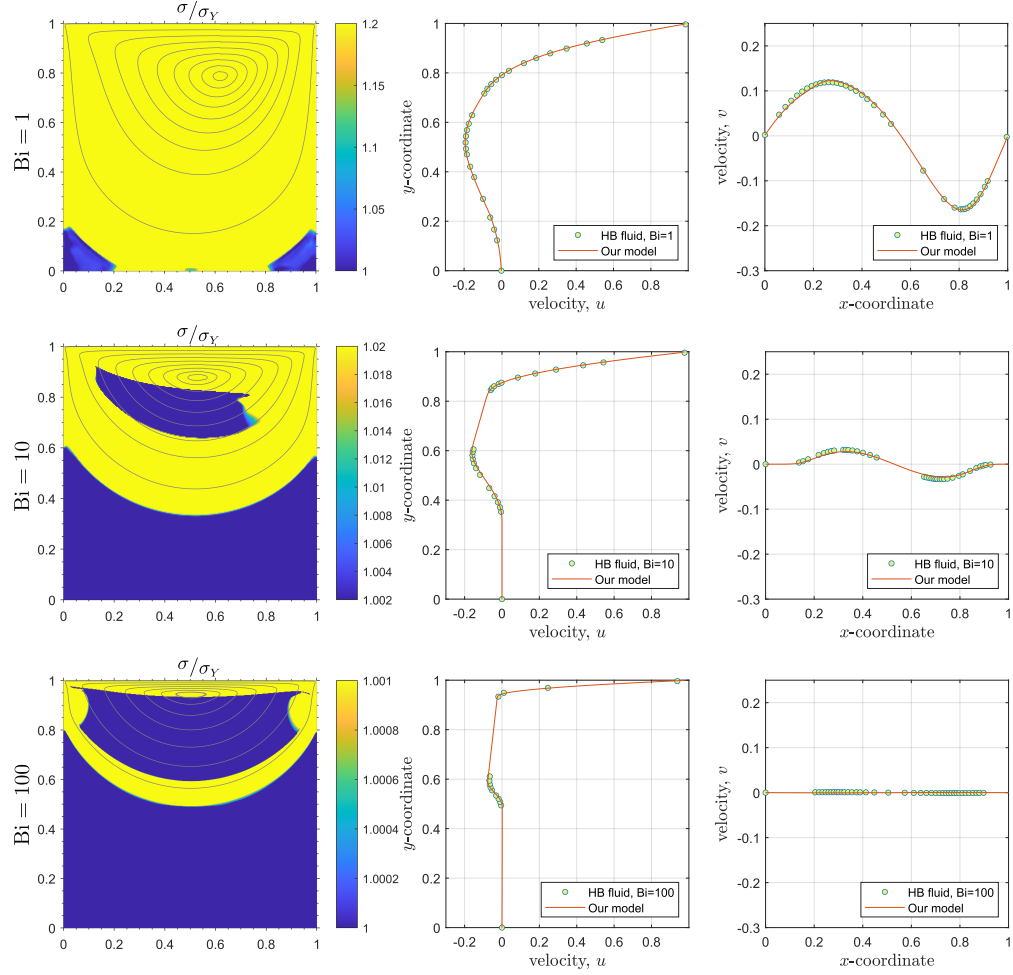


Figure 12: Lid-driven cavity flow of the GPR model in the elastoviscoplastic regime at  $Re = 100$  ( $\kappa = 10^{-2}$ ) and different Bingham numbers:  $Bi = 1$  (top row, final time  $t = 10$ ),  $Bi = 10$  (middle row, final time  $t = 1$ ), and  $Bi = 100$  (bottom row, final time  $t = 0.1$ ). Equivalent stress  $\sigma = \|\boldsymbol{\sigma}\|$  and streamlines (left column), and  $x = 0.5$  (middle column) and  $y = 0.5$  (right column) cuts of the velocity field compared against the solution to the Bingham model (data has been extracted from [79]). In the left column, the blue color correspond to the solidified regions.

possibility of quantitatively comparing the solution to the hyperbolic GPR model with the solution to the parabolic Navier-Stokes equations with the HB rheology, see the velocity cuts in Fig. 12. One can notice a good agreement with the reference solution. Also, we plot the snapshots of the velocity field in Fig. 13 in order to demonstrate that there is no flow in the solidified regions attached to the bottom of the cavity (the plug). The same computational meshes of  $256^2$  (for  $Bi = 1, 10$ ) and  $512^2$  (for  $Bi = 100$ ) were used for the case of  $Re = 100$ .

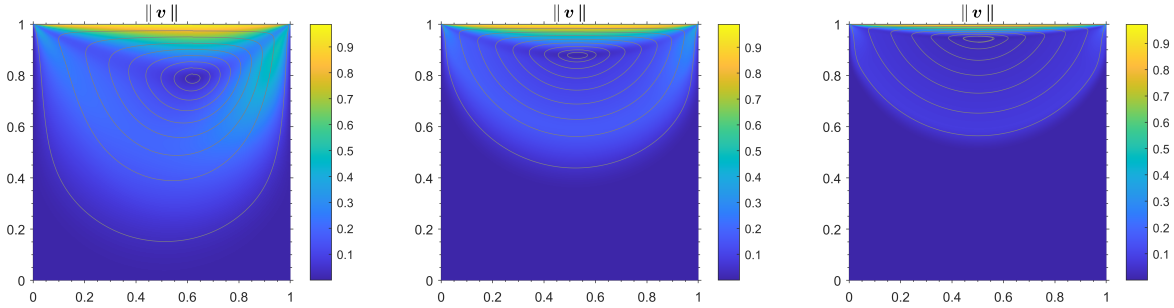


Figure 13: Lid-driven cavity flow of the GPR model in the elastoviscoplastic regime with  $n = 1$  at  $Re = 100$  and different  $Bi$  numbers:  $Bi = 1$  (left),  $Bi = 10$  (middle), and  $Bi = 100$  (right). The norm of the velocity field and streamlines showing the absence of the flow in the solidified region.

## 5. Conclusion and outlook

In this paper, we have studied the ability of the unified first-order hyperbolic model of continuum fluid and solid mechanics (2) to describe flows of non-Newtonian and, in particular, of viscoplastic fluids (or yield-stress fluids) [2]. Recently, it was already shown in [53] that the model can deal with non-Newtonian fluids with the power-law viscosity (without a yield stress), while here, for the first time, the model was used to describe the stress-driven solid-fluid transformations in the presence of the yield stress. Via direct comparison of the numerical solution of our model against analytical or numerical solutions to the Navier-Stokes equations with the Herschel-Bulkley viscosity on several standard benchmark test cases (Couette, Hagen-Poiseuille, and lid-driven cavity flows) it was demonstrated that the solution to the parabolic Navier-Stokes equations can be well approximated with the solution of our first-order hyperbolic model (2).

Note that, previously, the yield-stress fluids were modeled either with a pure viscous classical approach relying on the Navier-Stokes equations (Bingham-type models) and thus ignoring the elasticity of the unyielded state, or with more advanced elastoviscoplastic approaches which take into account the elasticity of the unyielded material [76, 77, 4, 39]. The latter, rely on the idea of additive splitting of the total Cauchy stress  $\boldsymbol{\sigma}$  into two parts  $\boldsymbol{\sigma}(\dot{\boldsymbol{\varepsilon}}, \boldsymbol{\varepsilon}) = \boldsymbol{\sigma}_{NS}(\dot{\boldsymbol{\varepsilon}}) + \boldsymbol{\sigma}_E(\boldsymbol{\varepsilon})$  with  $\boldsymbol{\sigma}_{NS}(\dot{\boldsymbol{\varepsilon}})$  being the conventional Navier-Stokes stress defined as the function of the strain rate  $\dot{\boldsymbol{\varepsilon}}$ , and  $\boldsymbol{\sigma}_E$  being the elastic stress which is a function of the strain  $\boldsymbol{\varepsilon}$ . The two stresses  $\boldsymbol{\sigma}_{NS}$  and  $\boldsymbol{\sigma}_E$  are conceptually different. Namely, the Navier-Stokes stress being the non-local stress (i.e. it involves the first gradient of the state vector) and fully dissipative in nature, while the elastic stress  $\boldsymbol{\sigma}_E$  being local and reversible. This makes it unclear the description of a general solid-fluid transformation (melting/solidification) with such an approach.

On the other hand, in our theory, the stress tensor, in both fluid and solid state, is computed in a unified manner  $\boldsymbol{\sigma} = -\rho \mathbf{A}^T E_{\mathbf{A}}$  based *only* on the strain measure, the distortion field  $\mathbf{A}$ , while the use of the strain rate  $\dot{\boldsymbol{\varepsilon}}$  is not required at all. This, we believe, is one of the main novelties of our theory in comparison with the conventional aforementioned approaches, which should make our approach attractive for modeling of processes involving general solid-fluid transformations including thermally-driven melting and solidification. Note that the heat conduction, being ignored in this study, can be also described by the first-order hyperbolic equations with relaxation-type source terms similar to (2c), see [62, 13, 31].

Because all the benchmark tests considered in this paper involve incompressible flows, we have employed our new Semi-Implicit Structure Preserving Finite Volume (SISPFV) scheme proposed in [13] which treats the pressure part



of the model in an implicit manner and thus, allows to run the model in the low-Mach number regime ( $Ma \rightarrow 0$ ). Further development of the scheme will concern an implicit treatment of the elastic part of the model which will allow to eliminate the shear sound speed from the stability condition of the numerical scheme resulting in a bigger time step. Also, in order to efficiently run the model in the stiff relaxation limit ( $\tau \ll 1$ ), we plan to incorporate an IMEX Runge-Kutta-type time-integration in order to improve the accuracy of the current SISPFV scheme in time. Furthermore, for better tracking of the yield surface in flows of viscoplastic fluids, or propagation of general solidification fronts, one could use Arbitrary Lagrangian-Eulerian (ALE) schemes [14, 15, 16] or even more general schemes on *non-conforming* meshes [41, 42, 18].

Further applications of the model will concern the modeling melting and solidification processes in additive manufacturing [36, 57, 56]. For this purposes we shall use our first-order hyperbolic model for heat conduction [62, 31, 13, 70] and hyperbolic surface tension model advanced by Gavrilyuk *et al* in [6] and further developed by Schmidmayer *et al* [78] and Chiochetti *et al* [26] in conjunction with a simple diffuse interface approach [84, 55, 18, 83, 40] for tracking the free boundaries.

## Acknowledgments

The research presented in this paper was partially funded by the European Union’s Horizon 2020 Research and Innovation Programme under the project *ExaHyPE*, grant no. 671698 (call FETHPC-1-2014). The authors also acknowledge funding from the Istituto Nazionale di Alta Matematica (INdAM) through the GNCS group and the program *Young Researchers Funding 2018* via the research project *Semi-implicit structure-preserving schemes for continuum mechanics*. E.R. acknowledges the financial support from the state contract of the Sobolev Institute of Mathematics (project no. 0314-2019-0012). Results by E.R. obtained in Sec.2 were done under the support of the Russian Science Foundation grant 19-77-20004. M.D., I.P., and S.C. acknowledge the financial support received from the Italian Ministry of Education, University and Research (MIUR) in the frame of the Departments of Excellence Initiative 2018–2022 attributed to DICAM of the University of Trento (grant L. 232/2016). S.C. acknowledges the financial support received by the Deutsche Forschungsgemeinschaft (DFG) under the project *Droplet Interaction Technologies (DROPIT)*, grant no. GRK 2160/1. W.B., M.D. and I.P. also received financial support in the frame of the PRIN Project 2017 *Innovative numerical methods for evolutionary partial differential equations and applications*. M.D. and I.P. have also received funding from the University of Trento via the *Strategic Initiative Modeling and Simulation* and via the *UniTN Starting Grant initiative*. I.P. acknowledges a partial support by ANR-11-LABX-0040-CIMI within the program ANR-11-IDEX-0002-02.

The authors are grateful to the Leibniz Rechenzentrum (LRZ) for awarding access to the SuperMUC supercomputer based in Munich, Germany.

## References

- [1] B. Andreotti, Y. Forterre, and O. Pouliquen. *Granular Media: Between Fluid and Solid*. Cambridge University Press, 2013, doi:10.1080/00107514.2014.885579.
- [2] N. J. Balmforth, I. A. Frigaard, and G. Ovarlez. Yielding to Stress : Recent Developments in Viscoplastic Fluid Mechanics. *Annual Review of Fluid Mechanics*, 46(August):121–146, 2014. doi:10.1146/annurev-fluid-010313-141424.
- [3] P. T. Barton, D. Drikakis, and E. I. Romenski. An Eulerian finite-volume scheme for large elastoplastic deformations in solids. *International Journal for Numerical Methods in Engineering*, 81:n/a–n/a, 2009, doi:10.1002/nme.2695.
- [4] S. Bénito, C. H. Bruneau, T. Colin, C. Gay, and F. Molino. An elasto-visco-plastic model for immortal foams or emulsions. *The European Physical Journal E*, 25(3):225–251, 2008, doi:10.1140/epje/i2007-10284-2.

- [5] A. Bermúdez, S. Busto, M. Dumbser, J. Ferrín, L. Saavedra, and M. Vázquez-Cendón. A staggered semi-implicit hybrid FV/FE projection method for weakly compressible flows. *Journal of Computational Physics*, 421:109743, 2020. doi:10.1016/j.jcp.2020.109743.
- [6] R. Berry, R. Saurel, F. Petitpas, E. Daniel, O. Métayer, and S. Gavrilyuk. Progress in the Development of Compressible , Multiphase Flow Modeling Capability for Nuclear Reactor Flow Applications. *Idaho National Laboratory*, (October), 2008. doi:10.2172/946849.
- [7] J. Bleyer, M. Maillard, P. De Buhan, and P. Coussot. Efficient numerical computations of yield stress fluid flows using second-order cone programming. *Computer Methods in Applied Mechanics and Engineering*, 283:599–614, 2015, doi:10.1016/j.cma.2014.10.008.
- [8] D. Bolmatov, V. V. Brazhkin, and K. Trachenko. Thermodynamic behaviour of supercritical matter. *Nature communications*, 4(2331):1–7, 2013, doi:10.1038/ncomms3331.
- [9] D. Bolmatov, D. Zav’yalov, M. Zhernenkov, E. T. Musaev, and Y. Q. Cai. Unified phonon-based approach to the thermodynamics of solid, liquid and gas states. *Annals of Physics*, 363:221–242, dec 2015, , doi:10.1016/j.aop.2015.09.018.
- [10] D. Bolmatov, M. Zhernenkov, D. Zav’yalov, S. Stoupin, Y. Q. Cai, and A. Cunsolo. Revealing the Mechanism of the Viscous-to-Elastic Crossover in Liquids. *The journal of physical chemistry letters*, 6(15):3048–3053, 2015.
- [11] W. Boscheri, G. Dimarco, R. Loubère, M. Tavelli, and M. Vignal. A second order all mach number imex finite volume solver for the three dimensional euler equations. *Journal of Computational Physics*, 415:109486, 2020.
- [12] W. Boscheri, G. Dimarco, and M. Tavelli. An efficient second order all mach finite volume solver for the compressible navier-stokes equations. *Comput. Methods Appl. Mech. Engrg.*, 374:113602, 2021.
- [13] W. Boscheri, M. Dumbser, M. Ioriatti, I. Peshkov, and E. Romenski. A structure-preserving staggered semi-implicit finite volume scheme for continuum mechanics. *Journal of Computational Physics*, 424:109866, jan 2021, doi:10.1016/j.jcp.2020.109866.
- [14] W. Boscheri and M. Dumbser. Arbitrary-Lagrangian-Eulerian One-Step WENO Finite Volume Schemes on Unstructured Triangular Meshes. *Communications in Computational Physics*, 14(5):1174–1206, nov 2013, doi:10.4208/cicp.181012.010313a.
- [15] W. Boscheri and M. Dumbser. A direct Arbitrary-Lagrangian–Eulerian ADER-WENO finite volume scheme on unstructured tetrahedral meshes for conservative and non-conservative hyperbolic systems in 3D. *Journal of Computational Physics*, 275:484–523, oct 2014, doi:10.1016/j.jcp.2014.06.059.
- [16] W. Boscheri, M. Dumbser, and O. Zanotti. High order cell-centered Lagrangian-type finite volume schemes with time-accurate local time stepping on unstructured triangular meshes. *Journal of Computational Physics*, 291:120–150, jun 2015, doi:10.1016/j.jcp.2015.02.052.
- [17] V. V. Brazhkin, Y. D. Fomin, A. G. Lyapin, V. N. Ryzhov, and K. Trachenko. Two liquid states of matter: A dynamic line on a phase diagram. *Physical Review E*, 85(3):031203, mar 2012, doi:10.1103/PhysRevE.85.031203.
- [18] S. Busto, S. Chiocchetti, M. Dumbser, E. Gaburro, and I. Peshkov. High order ADER schemes for continuum mechanics. *Frontiers in Physics*, 8:32, 2020. doi:10.3389/fphy.2020.00032.
- [19] S. Busto, J. Ferrín, E. Toro, and M. Vázquez-Cendón. A projection hybrid high order finite volume/finite element method for incompressible turbulent flows. *Journal of Computational Physics*, 353:169 – 192, 2018. doi:10.1016/j.jcp.2017.10.004.

- [20] S. Busto, G. Stabile, G. Rozza, and M. Vázquez-Cendón. POD–Galerkin reduced order methods for combined Navier–Stokes transport equations based on a hybrid FV–FE solver. *Computers and Mathematics with Applications*, 79:256–273, 2020. doi:10.1016/j.camwa.2019.06.026.
- [21] S. Busto, M. Tavelli, W. Boscheri, and M. Dumbser. Efficient high order accurate staggered semi-implicit discontinuous Galerkin methods for natural convection problems. *Computers and Fluids*, 198:104399, 2020. doi:10.1016/j.compfluid.2019.104399.
- [22] S. Busto, E. Toro, and E. Vázquez-Cendón. Design and analysis of ADER-type schemes for model advection–diffusion–reaction equations. *Journal of Computational Physics*, 327:553–575, 2016. doi:10.1016/j.jcp.2016.09.043.
- [23] M. E. Caplan, A. Giri, and P. E. Hopkins. Analytical model for the effects of wetting on thermal boundary conductance across solid/classical liquid interfaces. *The Journal of Chemical Physics*, 140(15):154701, apr 2014, doi:10.1063/1.4870778.
- [24] V. Casulli and P. Zanolli. A Nested Newton-Type Algorithm for Finite Volume Methods Solving Richards’ Equation in Mixed Form. *SIAM Journal on Scientific Computing*, 32(4):2255–2273, jan 2010, doi:10.1137/100786320.
- [25] V. Casulli and P. Zanolli. Iterative solutions of mildly nonlinear systems. *Journal of Computational and Applied Mathematics*, 236(16):3937–3947, oct 2012, doi:10.1016/j.cam.2012.02.042.
- [26] S. Chiocchetti, I. Peshkov, S. Gavriluk, and M. Dumbser. High order ADER schemes and GLM curl cleaning for a first order hyperbolic formulation of compressible flow with surface tension. *Journal of Computational Physics*, page 109898, oct 2021, , doi:10.1016/j.jcp.2020.109898.
- [27] M. Dumbser, D. Balsara, M. Tavelli, and F. Fambri. A divergence-free semi-implicit finite volume scheme for ideal, viscous, and resistive magnetohydrodynamics. *International Journal for Numerical Methods in Fluids*, 89(1-2):16–42, jan 2019, , doi:10.1002/flid.4681.
- [28] M. Dumbser and V. Casulli. A conservative, weakly nonlinear semi-implicit finite volume scheme for the compressible Navier- with general equation of state. *Applied Mathematics and Computation*, 272(M):479–497, jan 2016, doi:10.1016/j.amc.2015.08.042.
- [29] M. Dumbser, C. Enaux, and E. F. Toro. Finite volume schemes of very high order of accuracy for stiff hyperbolic balance laws. *Journal of Computational Physics*, 227(8):3971–4001, apr 2008, doi:10.1016/j.jcp.2007.12.005.
- [30] M. Dumbser, I. Peshkov, and E. Romenski. A Unified Hyperbolic Formulation for Viscous Fluids and Elastoplastic Solids. In C. Klingenberg and M. Westdickenberg, editors, *Theory, Numerics and Applications of Hyperbolic Problems II. HYP 2016*, volume 237 of *Springer Proceedings in Mathematics and Statistics*, pages 451–463. Springer International Publishing, Cham, 2018, doi:10.1007/978-3-319-91548-7\_34.
- [31] M. Dumbser, I. Peshkov, E. Romenski, and O. Zanotti. High order ADER schemes for a unified first order hyperbolic formulation of continuum mechanics: Viscous heat-conducting fluids and elastic solids. *Journal of Computational Physics*, 314:824–862, jun 2016, , doi:10.1016/j.jcp.2016.02.015.
- [32] M. Dumbser, I. Peshkov, E. Romenski, and O. Zanotti. High order ADER schemes for a unified first order hyperbolic formulation of Newtonian continuum mechanics coupled with electro-dynamics. *Journal of Computational Physics*, 348:298–342, nov 2017, , doi:10.1016/j.jcp.2017.07.020.
- [33] M. Dumbser, O. Zanotti, A. Hidalgo, and D. S. Balsara. ADER-WENO finite volume schemes with space–time adaptive mesh refinement. *Journal of Computational Physics*, 248:257–286, sep 2013. doi:10.1016/j.jcp.2013.04.017.

- [34] F. Fambri. Discontinuous Galerkin Methods for Compressible and Incompressible Flows on Space–Time Adaptive Meshes: Toward a Novel Family of Efficient Numerical Methods for Fluid Dynamics. *Archives of Computational Methods in Engineering*, jan 2019, doi:10.1007/s11831-018-09308-6.
- [35] F. Fambri, M. Dumbser, and O. Zanotti. Space–time adaptive ADER-DG schemes for dissipative flows: Compressible Navier–Stokes and resistive MHD equations. *Computer Physics Communications*, 220:297–318, nov 2017, doi:10.1016/j.cpc.2017.08.001.
- [36] M. Francois, A. Sun, W. King, N. Henson, D. Tourret, C. Bronkhorst, N. Carlson, C. Newman, T. Haut, J. Bakosi, J. Gibbs, V. Livescu, S. Vander Wiel, A. Clarke, M. Schraad, T. Blacker, H. Lim, T. Rodgers, S. Owen, F. Abdeljawad, J. Madison, A. Anderson, J.-L. Fattebert, R. Ferencz, N. Hodge, S. Khairallah, and O. Walton. Modeling of additive manufacturing processes for metals: Challenges and opportunities. *Current Opinion in Solid State and Materials Science*, 21(4):198–206, aug 2017, doi:10.1016/j.cossms.2016.12.001.
- [37] M. Frank and D. Drikakis. Thermodynamics at Solid–Liquid Interfaces. *Entropy*, 20(5):362, may 2018, doi:10.3390/e20050362.
- [38] J. Frenkel. *Kinetic theory of liquids*. Dover, New York, NY, 1955.
- [39] L. Fusi and A. Farina. Modelling of Bingham-like fluids with deformable core. *Computers and Mathematics with Applications*, 53(3-4):583–594, 2007. doi:10.1016/j.camwa.2006.02.033.
- [40] A.-A. Gabriel, D. Li, S. Chiocchetti, M. Tavelli, I. Peshkov, E. Romenski, and M. Dumbser. A unified first order hyperbolic model for nonlinear dynamic rupture processes in diffuse fracture zones. *Philosophical Transactions of the Royal Society A*, jul 2021, , doi:10.1098/rsta.2020.0130.
- [41] E. Gaburro. A Unified Framework for the Solution of Hyperbolic PDE Systems Using High Order Direct Arbitrary-Lagrangian–Eulerian Schemes on Moving Unstructured Meshes with Topology Change. *Archives of Computational Methods in Engineering*, feb 2020, doi:10.1007/s11831-020-09411-7.
- [42] E. Gaburro, W. Boscheri, S. Chiocchetti, C. Klingenberg, V. Springel, and M. Dumbser. High order direct Arbitrary-Lagrangian-Eulerian schemes on moving Voronoi meshes with topology changes. *Journal of Computational Physics*, 407:109167, apr 2020, doi:10.1016/j.jcp.2019.109167.
- [43] S. Gavriluk, N. Favrie, and R. Saurel. Modelling wave dynamics of compressible elastic materials. *Journal of Computational Physics*, 227(5):2941–2969, feb 2008, doi:10.1016/j.jcp.2007.11.030.
- [44] S. K. Godunov and I. M. Peshkov. Thermodynamically consistent nonlinear model of elastoplastic Maxwell medium. *Computational Mathematics and Mathematical Physics*, 50(8):1409–1426, aug 2010, doi:10.1134/S0965542510080117.
- [45] S. K. Godunov and E. I. Romenskii. Nonstationary equations of nonlinear elasticity theory in eulerian coordinates. *Journal of Applied Mechanics and Technical Physics*, 13(6):868–884, nov 1972, doi:10.1007/BF01200547.
- [46] S. K. Godunov and E. I. Romenskii. *Elements of continuum mechanics and conservation laws*. Kluwer Academic/Plenum Publishers, 2003.
- [47] S. Godunov. *Elements of Continuum Mechanics [in Russian]*. Nauka, Moscow, 1978.
- [48] M. Grmela. A framework for elasto-plastic hydrodynamics. *Physics Letters A*, 312(3-4):136–146, jun 2003, doi:10.1016/S0375-9601(03)00565-6.
- [49] S. Hank, N. Favrie, and J. Massoni. Modeling hyperelasticity in non-equilibrium multiphase flows. *Journal of Computational Physics*, 330(November):65–91, feb 2017, doi:10.1016/j.jcp.2016.11.001.

- [50] S. Hank, S. Gavriluk, N. Favrie, and J. Massoni. Impact simulation by an Eulerian model for interaction of multiple elastic-plastic solids and fluids. *International Journal of Impact Engineering*, 109:104–111, nov 2017, doi:10.1016/j.ijimpeng.2017.06.003.
- [51] F. W. Hehl and Y. N. Obukhov. Elie Cartan’s torsion in geometry and in field theory, an essay. *Annales de la Fondation Louis de Broglie*, 32(2-3):157–194, nov 2007,
- [52] Y. Heo, M. Antoaneta Bratescu, D. Aburaya, and N. Saito. A phonon thermodynamics approach of gold nanofluids synthesized in solution plasma. *Applied Physics Letters*, 104(11):111902, mar 2014, doi:10.1063/1.4868872.
- [53] H. Jackson and N. Nikiforakis. A numerical scheme for non-Newtonian fluids and plastic solids under the GPR model. *Journal of Computational Physics*, 387:410–429, jun 2019, , doi:10.1016/j.jcp.2019.02.025.
- [54] L. Jacob. *Plasticity theory / Jacob Lubliner*. Macmillan Publishing Company, New York, C 1990.
- [55] F. Kemm, E. Gaburro, F. Thein, and M. Dumbser. A simple diffuse interface approach for compressible flows around moving solids of arbitrary shape based on a reduced Baer–Nunziato model. *Computers & Fluids*, 204:104536, may 2020, doi:10.1016/j.compfluid.2020.104536.
- [56] S. A. Khairallah, A. T. Anderson, A. Rubenchik, and W. E. King. Laser powder-bed fusion additive manufacturing: Physics of complex melt flow and formation mechanisms of pores, spatter, and denudation zones. *Acta Materialia*, 108:36–45, apr 2016, doi:10.1016/j.actamat.2016.02.014.
- [57] W. E. King, A. T. Anderson, R. M. Ferencz, N. E. Hodge, C. Kamath, S. A. Khairallah, and A. M. Rubenchik. Laser powder bed fusion additive manufacturing of metals; physics, computational, and materials challenges. *Applied Physics Reviews*, 2(4):041304, dec 2015, doi:10.1063/1.4937809.
- [58] S. Klainermann and A. Majda. Singular limits of quasilinear hyperbolic systems with large parameters and the incompressible limit of compressible fluid. *Communications on Pure and Applied Mathematics*, 34:481–524, 1981.
- [59] S. Klainermann and A. Majda. Compressible and incompressible fluids. *Communications on Pure and Applied Mathematics*, 35:629–651, 1982.
- [60] R. Klein, N. Botta, T. Schneider, C. Munz, S. Roller, A. Meister, L. Hoffmann, and T. Sonar. Asymptotic adaptive methods for multi-scale problems in fluid mechanics. *Journal of Engineering Mathematics*, 39:261–343, 2001.
- [61] J. Málek, V. Průša, and K. Rajagopal. Generalizations of the Navier–Stokes fluid from a new perspective. *International Journal of Engineering Science*, 48(12):1907–1924, dec 2010, doi:10.1016/j.ijengsci.2010.06.013.
- [62] A. N. Malyshev and E. I. Romenskii. Hyperbolic equations for heat transfer. Global solvability of the Cauchy problem. *Siberian Mathematical Journal*, 27(5):734–740, 1987, doi:10.1007/BF00969202.
- [63] C. Munz, S. Roller, R. Klein, and K. Geratz. The extension of incompressible flow solvers to the weakly compressible regime. *Computers and Fluids*, 32:173–196, 2003.
- [64] L. Pareschi and G. Russo. Implicit-explicit Runge-Kutta schemes for stiff systems of differential equations. *Advances in the Theory of Computational Mathematics*, 3:269–288, 2000.
- [65] L. Pareschi and G. Russo. Implicit-explicit Runge-Kutta schemes and applications to hyperbolic systems with relaxation. *Journal of Scientific Computing*, 25:129–155, 2005.
- [66] M. Pavelka, V. Klika, and M. Grmela. *Multiscale Thermo-Dynamics*. De Gruyter, Berlin, Boston, aug 2018, doi:10.1515/9783110350951.

- [67] P. Perzyna. Fundamental Problems in Viscoplasticity. *Advances in Applied Mechanics*, 9:243–377, 1966, doi:10.1016/S0065-2156(08)70009-7.
- [68] I. Peshkov, W. Boscheri, R. Loubère, E. Romenski, and M. Dumbser. Theoretical and numerical comparison of hyperelastic and hypoelastic formulations for Eulerian non-linear elastoplasticity. *Journal of Computational Physics*, 387:481–521, jun 2019, , doi:10.1016/j.jcp.2019.02.039.
- [69] I. Peshkov, M. Grmela, and E. Romenski. Irreversible mechanics and thermodynamics of two-phase continua experiencing stress-induced solid–fluid transitions. *Continuum Mechanics and Thermodynamics*, 27(6):905–940, nov 2015, doi:10.1007/s00161-014-0386-1.
- [70] I. Peshkov, M. Pavelka, E. Romenski, and M. Grmela. Continuum mechanics and thermodynamics in the Hamilton and the Godunov-type formulations. *Continuum Mechanics and Thermodynamics*, 30(6):1343–1378, nov 2018, , doi:10.1007/s00161-018-0621-2.
- [71] I. Peshkov and E. Romenski. A hyperbolic model for viscous Newtonian flows. *Continuum Mechanics and Thermodynamics*, 28(1-2):85–104, mar 2016, doi:10.1007/s00161-014-0401-6.
- [72] I. Peshkov, E. Romenski, and M. Dumbser. Continuum mechanics with torsion. *Continuum Mechanics and Thermodynamics*, 31(5):1517–1541, sep 2019, , doi:10.1007/s00161-019-00770-6.
- [73] A. M. V. Putz and T. I. Burghlea. The solid–fluid transition in a yield stress shear thinning physical gel. *Rheologica Acta*, 48(6):673–689, jul 2009, doi:10.1007/s00397-009-0365-9.
- [74] E. Romenski, I. Peshkov, M. Dumbser, and F. Fambri. A new continuum model for general relativistic viscous heat-conducting media. *Philosophical Transactions of the Royal Society A: Mathematical, Physical and Engineering Sciences*, 378(2170):20190175, may 2020, , doi:10.1098/rsta.2019.0175.
- [75] E. I. Romenskii. Dynamic three-dimensional equations of the Rakhmatulin elastic-plastic model. *Journal of Applied Mechanics and Technical Physics*, 20(2):229–244, 1979. doi:10.1007/BF00910025.
- [76] P. Saramito. A new constitutive equation for elastoviscoplastic fluid flows. *Journal of Non-Newtonian Fluid Mechanics*, 145(1):1–14, 2007. doi:10.1016/j.jnnfm.2007.04.004.
- [77] P. Saramito. A new elastoviscoplastic model based on the Herschel–Bulkley viscoplastic model. *Journal of Non-Newtonian Fluid Mechanics*, 158(1-3):154–161, may 2009, doi:10.1016/j.jnnfm.2008.12.001.
- [78] K. Schmidmayer, F. Petitpas, E. Daniel, N. Favrie, and S. Gavriluk. A model and numerical method for compressible flows with capillary effects. *Journal of Computational Physics*, 334:468–496, 2017, doi:10.1016/j.jcp.2017.01.001.
- [79] K. Sverdrup, N. Nikiforakis, and A. Almgren. Highly parallelisable simulations of time-dependent viscoplastic fluid flow with structured adaptive mesh refinement. *Physics of Fluids*, 30(9):093102, sep 2018, , doi:10.1063/1.5049202.
- [80] A. Syrakos, G. C. Georgiou, and A. N. Alexandrou. Performance of the finite volume method in solving regularised Bingham flows: Inertia effects in the lid-driven cavity flow. *Journal of Non-Newtonian Fluid Mechanics*, 208-209:88–107, jun 2014, , doi:10.1016/j.jnnfm.2014.03.004.
- [81] M. Tavelli and M. Dumbser. A staggered space–time discontinuous Galerkin method for the incompressible Navier–Stokes equations on two–dimensional triangular meshes. *Computers and Fluids*, 119:235–249, 2015.
- [82] M. Tavelli and M. Dumbser. A pressure-based semi-implicit space-time discontinuous Galerkin method on staggered unstructured meshes for the solution of the compressible Navier–Stokes equations at all Mach numbers. *Journal of Computational Physics*, 341:341–376, 2017.

- [83] M. Tavelli, S. Chiocchetti, E. Romenski, A.-A. Gabriel, and M. Dumbser. Space-time adaptive ADER discontinuous Galerkin schemes for nonlinear hyperelasticity with material failure. *Journal of Computational Physics*, 422:109758, 2020, , doi:[10.1016/j.jcp.2020.109758](https://doi.org/10.1016/j.jcp.2020.109758).
- [84] M. Tavelli, M. Dumbser, D. E. Charrier, L. Rannabauer, T. Weinzierl, and M. Bader. A simple diffuse interface approach on adaptive Cartesian grids for the linear elastic wave equations with complex topography. *Journal of Computational Physics*, 386:158–189, jun 2019, doi:[10.1016/j.jcp.2019.02.004](https://doi.org/10.1016/j.jcp.2019.02.004).
- [85] V. Titarev and E. Toro. ADER: Arbitrary high order Godunov approach. *Journal of Scientific Computing*, 17(1-4):609–618, 2002.
- [86] V. Titarev and E. Toro. ADER schemes for three-dimensional nonlinear hyperbolic systems. *Journal of Computational Physics*, 204:715–736, 2005.
- [87] E. F. Toro. *Riemann Solvers and Numerical Methods for Fluid Dynamics*. Springer, third edition, 2009.
- [88] E. F. Toro, R. C. Millington, and L. A. M. Nejad. Towards very high order {Godunov} schemes. In E. F. Toro, editor, *Godunov Methods. Theory and Applications*, pages 905–938. Kluwer/Plenum Academic Publishers, 2001.
- [89] E. F. Toro and V. A. Titarev. Derivative Riemann solvers for systems of conservation laws and ADER methods. *Journal of Computational Physics*, 212(1):150–165, 2006.
- [90] E. Toro and V. Titarev. Solution of the generalized Riemann problem for advection-reaction equations. *Proc. Roy. Soc. London*, pages 271–281, 2002.
- [91] E. Toro and M. Vázquez-Cendón. Flux splitting schemes for the Euler equations. *Computers and Fluids*, 70:1–12, 2012. doi:<https://doi.org/10.1016/j.compfluid.2012.08.023>.